Linköping Studies in Science and Technology
Dissertation No. 1070

On optical methods for intracerebral measurements during stereotactic and functional neurosurgery

– Experimental studies

Johan Antonsson

Linköping University
INSTITUTE OF TECHNOLOGY

Department of Biomedical Engineering
Division of Biomedical Instrumentation
Linköpings universitet
SE-58185 Linköping, Sweden

On optical methods for intracerebral measurements
during stereotactic and functional neurosurgery
-Experimental studies

Department of Biomedical Engineering
Linköping University
SE-581 85 Linköping,Sweden

ISBN 978-91-85715-91-6 ISSN 0345-7524

Printed in Linköping , Sweden
by LiU-Tryck Linköping, 2007

To Anette
and our children

Abstract

Radio frequency (RF) lesioning and deep brain stimulation (DBS) are the two prevailing surgical treatments for movement disorders within the field of stereotactic and functional neurosurgery. For RF-lesioning, a small volume of brain tissue is coagulated and knowledge of the lesion size and growth is of great importance for the safety and outcome of the procedure. This thesis deals with adapting the laser Doppler perfusion monitoring (LDPM) technique for measurements in brain tissue during RF-lesioning. The relation between LDPM signal changes and developed lesion size was investigated. LDPM measurements were evaluated both *in vitro* (albumin protein solution) and *in vivo* in the porcine brain during RF-lesioning corresponding to a bilateral thalamotomy in man. The investigated signals from the LDPI measurements can be used for following the lesioning time course and to detect if a lesion was created, both *in vitro* and in the animal model. For the albumin model, both the total backscattered light intensity and the perfusion signal can be used as markers for estimating the final coagulation size, while in the animal model this conclusion was not statistical verified.

Independent on surgical method, RF-lesioning or DBS, intracerebral guidance is an important aspect within stereotactic and functional neurosurgery. To increase the accuracy and precision of reaching the correct target, different methods for intracerebral guidance exist, such as microelectrode recording and impedance methods. In this thesis, the possibility of developing an optical intracerebral guidance method has been investigated. Diffuse reflectance spectroscopy served as technology and all measurements were performed stereotactically in both porcine and human brain. Measurements of white and gray matter showed large differences, with higher reflectivity for white brain matter, both in porcine and in human brain. For the human measurements during DBS-implants, large differences between white matter and functional targets were found. Additionally, differences between native and lesioned porcine brain matter were detected. Both studies support the idea of using diffuse reflectance spectroscopy for developing an intracerebral guidance method.

List of papers

This thesis is based on the following papers, which are referred to in the text by their Roman numerals.

I. Antonsson, J., Eriksson, O., and Wårdell, K., *Radio frequency electrode system for optical lesion size estimation in functional neurosurgery.* Journal of Biomedical Optics, 2005. **10**(3): p. 1-6.
II. Antonsson, J., Eriksson, O., Lundberg, P., and Wårdell, K., *Optical measurements during experimental stereotactic radiofrequency lesioning.* Stereotact Funct Neurosurg, 2006. **84**(2-3): p. 118-24.
III. Antonsson, J., Eriksson, O., and Wårdell, K., *In-vivo reflection spectroscopy measurements in pig brain during stereotactic surgery.* Proceedings of SPIE, 2003. **4958**: p. 242-250.
IV. Antonsson, J., Eriksson, O., Blomstedt, P., Bergenheim, A. T., Hariz, M., Richter, J., Zsigmond, P., and Wårdell, K., *Diffuse reflectance spectroscopy measurements for tissue type discrimination during deep brain stimulation*. Submitted.
V. Yavari, N., Dam, S., Antonsson, J., Wårdell, K., and Anderson-Engels, S., *In vitro measurements of optical properties of porcine brain using a novel compact device.* Med Biol Eng Comput, 2005. **43**(5): p. 658-66.

Abbreviations

AC-PC - Anterior Commissure - Posterior Commissure
CASH - Combined Angular and Spatial resolved Head
CT - Computed Tomography
DBS - Deep Brain Stimulation
GPe - Globus Pallidus externa
GPi - Globus Pallidus interna
LDF - Laser Doppler Flowmetry
LDPI - Laser Doppler Perfusion Imaging
LDPM - Laser Doppler Perfusion Monitoring
LNG - Leksell® Neuro Generator
LSS - Leksell® Stereotactic System
MER – Microelectrode recoording
MRI - Magnetic Resonance Imaging
PD - Parkinson's Disease
RF - Radio Frequency
SN - Substantia Nigra
STN - Subthalamic Nucleus
Vim - Ventral intermedius nucleus
VPL - Ventral Posteriolateral thalamus
VPM - Ventral Posterio Medial thalamus
Zi - Zona Incerta

Contents

1 Introduction

This thesis deals mainly with two different optical methods, laser Doppler perfusion monitoring (LDPM) and diffuse reflectance spectroscopy, applied during stereotactic and functional neurosurgery. The thesis focus is on experiments, ranging from the laboratory via animals to measurements in the human brain during clinical neurosurgery. By performing functional neurosurgery in a selected target area deep inside the brain, the patient's specific symptoms can be suppressed. However, unwanted side effects, both transient and persistent, may occur [1].

Patients suffering from degenerative movement disorders have been subjects for stereotactic and functional neurosurgery since the 1940:s [2, 3]. The traditional method, more rarely used in industrial countries today, is radio frequency (RF) lesioning [4], while the most common and widely used method is deep brain stimulation (DBS) [5]. During RF-lesioning, the patients' symptoms are suppressed by the destruction/coagulation of a small tissue volume in the deeper parts of the brain, while during DBS, a small flexible electrode delivers an alternating current from an implanted DBS-electrode.

In RF-lesioning, the growth and final size of the lesions are of the utmost importance for the clinical outcome. Today, no methods exist for intraoperative lesion size estimation, merely postoperative investigations. With more knowledge of the lesion development and the final size, the procedures could be performed more safely.

When performing RF-lesioning in brain tissue, the optical properties of the tissue change and blood flow disappears in the lesioned volume [6]. By applying optical methods such as laser Doppler perfusion monitoring, these changes could be used for studying the lesioning process. The changes in blood flow and optical properties could also be related to the lesion growth and possibly to the final size.

Independent of surgical method (RF or DBS), finding the correct target position inside the brain during stereotactic neurosurgery is crucial for the outcome. Even with better understanding of the human brain and refined imaging technology, the basic need for intracerebral guidance support is great. Today, the surgeon relies on MR or CT images acquired in the planning stage of the procedure [7]. While during surgery, complications such as brain shift and target miscalculations from the pre-surgical image investigation affect the precision [8].

Differences in optical properties between white and gray brain matter have previously been investigated [9, 10]. Such differences could be suitable for tissue discrimination, and by applying diffuse reflectance spectroscopy measurements at neurosurgery, a new intracerebral guidance method might be developed. In this thesis, the emphasis has been on RF-lesioning and intracerebral guidance, using two different optical measurement techniques.

2 Neurosurgical background

2.1 The human brain

The human brain is a remarkable organ. It controls body movements, posture, houses thoughts and emotions. All this centered in just one small organ having a weight of about 1.2-1.4 kg, while consuming approximately 20 % of the cardiac output and 20 % of the oxygen at rest. The central nervous system consists of the brain and the spinal cord together, and contains approximately 10^{11} neurons and 10^{12} neuroglia. On average, each nerve cell has 10^3 synaptic connections, which results in a total of approximately 10^{14}-10^{15} synaptic connections in the human brain [11].

Brain tissue can be categorized as gray matter consisting of nerve-cell bodies together with neuroglia cells, and white matter mainly consisting of myelined axons. The high amount of lipids in the myelin structures makes white brain tissue appear brighter than gray matter. The fat/lipid content is typically 5-8 % in gray matter and approximately 17-18 % in white matter [12, 13]. The lipid concentration differs between individuals and according to gender and age. The myelin sheets wrapped around the axon increase the propagation speed of electrical impulses, by acting as an electrical insulator, saltatory conduction. Neuroglia cells, often called the supporting matrix for the brain neurons, have additional roles such as metabolic support functions, and to keep the chemical balance [14].

The blood supply of the brain is of the utmost importance, only 10 s of ischemia can cause unconsciousness. A dense capillary network delivers well oxygenated blood to the whole brain structure. The capillary density in gray matter is approximately 2-3 times higher than in white. In gray matter, no neuron is more than 100 µm from a capillary. Perfusion values of 47-94 ml/(100g*min) in gray matter, and 20-25 ml/(100g*min) in white matter have been reported [14-16].

An overview of the brain usually mentions the complex blood-brain barrier. This barrier protects the brain from unwanted substances. The principle is to keep the cerebrospinal fluid separated from the normal blood stream, and thereby protect the brain. A part of the blood-brain barrier is located in the endothelial cells in the capillary wall, where the substance transport is both active and passive.

Lipid soluble substances can easily diffuse across the barrier, while glucose is actively transported across the capillary walls, but similar-sized and shaped molecules cannot [11, 14].

The brain has three major parts, the cerebrum, cerebellum and the brainstem, where the cerebrum contains the functional targets described in this thesis. The cortex, at the surface of the cerebrum, is a thin (2-4 mm thick) strongly folded gray surface, with the approximate surface size of 2400 cm^2 [11, 17]. Underneath this layer, the brain consists mostly of myelined axons, (white tissue). The deep brain structures in the center of the cerebrum, are a collection of gray nuclei surrounded by areas of white matter, often referred to as the basal ganglia and the thalamus [18]. This part of the brain houses the target areas that are applicable for functional neurosurgery.

2.1.1 The basal ganglia and thalamus

The basal ganglia consist of caudate nucleus, putamen, globus pallidus interna and externa (GPi and GPe), substantia nigra (SN), and subthalamic nucleus (STN), Figure 1. Different nomenclature exists in the literature; however, the described classification of the basal ganglia is common. The STN serves as input to the basal ganglia, while GPi and SN serve as the output towards the thalamus and the brainstem [19].

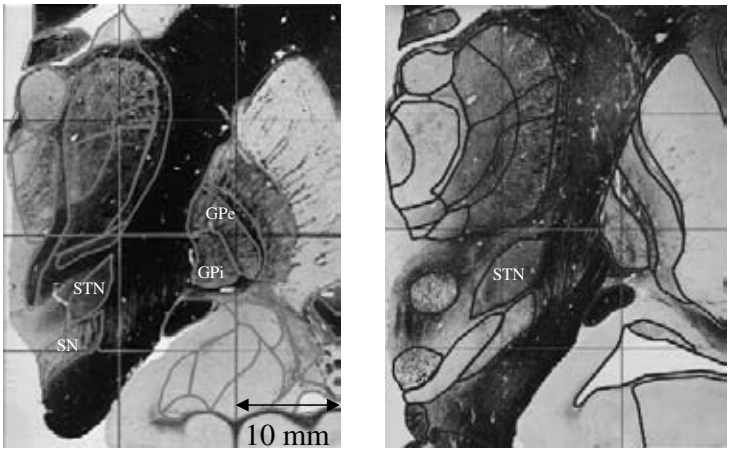

Figure 1. Overview of basal ganglia and thalamus from the Schaltenbrand-Wharen atlas (The Clinical Cerefy™ Brain Atlas). The presented area contains targets which are the most common in functional neurosurgery especially for movement disorders. a) Coronal +2 mm, b) coronal -3 mm.

The thalamus is a large volume of gray matter, approximately 3 cm long, oval shaped, consisting of several important nuclei. The basal ganglia nuclei surround the thalamus. Principally, projections from the cortex into the basal ganglia and thalamus are both back-projected to the cortex and relayed to the brainstem. These projections are involved in cognitive functions, posture and motor control. The complex network relationship between different nuclei in the basal ganglia and thalamus use both inhibition and excitation of the nerve signals propagating through the area. A precise balance between all these connections is necessary for the functionality of motor control. The complex behavior of different nerve signals propagating through this area is subject to extensive research, but still not completely understood [18-20].

The preferred choice of surgical targets in the basal ganglia and thalamus depends on the patient's symptoms and diagnosis. Patients, mainly suffering from resting tremor, usually benefit from surgery in different parts of the thalamus [5, 21]. Other common targets in thalamus, preferable for pain reduction surgery, are ventral posterolateral and ventral posteromedial nucleus (VPL and VPM) [22].

Except for the targets, the anterior commissure (AC) and posterior commissure (PC) are important anatomical landmarks during functional neurosurgery. These are neural interconnections between the two brain hemispheres, easily detected from MRI investigations. The imaginary line between these commissures (AC-PC line), calculated from MRI, is particularly useful for guidance in the brain. The AC-PC line has roughly the same length in all humans (24-28 mm) and the target coordinates are calculated in relation to the AC-PC line [14, 23].

With MRI it is possible to visually identify the target areas in the Gpi and the STN. Concerning the target areas in the thalamus these can not be visualized, why these have to be identified from statistical atlas coordinates. When identifying a target from an atlas the coordinates are calculated from the anterior and the posterior commissure. These two structures are the landmarks from which the brain is divided by three intersecting perpendicular planes into a Cartesian coordinate system.

2.1.2 Movement disorders and Parkinson's disease

The categorization of degenerative movement disorders as hypokinetic or hyperkinetic[1] is common [19, 20]. One example of a hypokinetic disorder is Parkinson's disease, while Tourette's syndrome, dystonia, hemiballism and drug-induced dyskinesia are hyperkinetic examples.

Parkinson's disease (PD) is a well-known disease in the group of degenerative neurological movement disorders. In Sweden, approximately 1 % of the elderly population suffers from this disease [24]. Approximately the same prevalence of PD patients can be found in other countries [25]. In PD patients, the loss of dopamine producing neurons causes a disturbance in the basal ganglia. These neurons normally project the neural activity from substantia nigra to the putamen [18]. The neurotransmitter dopamine works as an inhibitor to reduce the basal ganglia output. The loss of these cells results in an over-activity of the motor pathways output and displays as the PD symptoms of tremor, cogwheel rigidity, akinesia, bradykinesia, and loss of body control [19, 26]. Tremor is involuntary muscle contractions where the limbs are shaking, while rigidity is stiffness in movements. Cogwheel rigidity displays when the limbs stop and start for short moments. Akinesia is the problem of initiating movements and finally bradykinesia, when the patient's movements are reduced in size and slowed down.

Parkinsonian patients with bradykinesia are most likely to benefit from STN-DBS [19], while the best effect concerning dystonia normally is achieved in Gpi [27]. Tremor of various origins usually benefits most from surgery in the thalamus ventralis intermedius nucleus (Vim) [28] and zona incerta (Zi) [29].

In the 1940-50s, ablative neurosurgical treatment was introduced in the thalamus and pallidum and a rapid development took place [30]. In 1968, the role of dopamine was discovered. Dopamine can unfortunately not be delivered to the brain due to the blood-brain barrier, and the precursor drug L-dopa was developed to solve this problem. L-dopa became the preferable alternative to neurosurgery [18, 31]. A dormant period followed and neurosurgical procedures became less common [32]. However, due to the large dosage of L-dopa in PD patients it was found that patients often experienced side effects from the medication. Examples are depressions [33], drug-resistance after years of usage [34] and drug induced symptoms. Neurosurgical procedures (both ablative and deep brain stimulation) in the basal ganglia and thalamus were rediscovered in the 1980-90s. A combination of imaging advancements such as MRI together

[1] In patients with hyperkinetic movement disorders, the movements are involuntary and excessive while hypokinetic movements are reduced in size or slowed down.

with the rediscovering of old neurosurgical techniques, boosted the stereotactic and functional neurosurgical field [4, 34].

2.2 Stereotactic and functional neurosurgery

The word stereotactic originates from the Greek word *stereo* - three-dimensional and the Latin word *tactus* - to touch. The word functional refers to the alteration of a function. By this definition, stereotactic and functional neurosurgery implies reaching a position using three-dimensional orientation inside the human brain, and finally to alter the functionality of the reached target.

When using present imaging techniques[2], the targets in functional neurosurgery are "invisible"; the actual position of a target is individual and can even be different between the two hemispheres within one patient. In addition, the target can shift slightly when opening up the skull (brain shift). Hence, stereotactic and functional neurosurgery aims at finding the correct target safely with high accuracy, and well in place, to perform the most beneficial treatment.

Except for the two standard neurosurgical methods, radio frequency lesioning and deep brain stimulation, extensive research in gene therapy together with the implantation of stem cells and xenotype cells [35-37] are undergoing progress. Research has also been conducted on the implantation of Dopamine-producing fetus cells [38-40]. However, none of these methods has yet proven to be useful in a large-scale clinical environment, although they are of great interest.

2.2.1 Stereotactic frames and targeting principles

In 1908 the first true stereotactic frame for animal use was constructed [41], and in 1947 the first frame for clinical use was developed [2]. These first stereotactic frames were translational systems, meaning that there was no possibility to choose trajectory angles for the instruments, only coordinates. Today both frame-based and frameless stereotactic systems exist to guide and support the instruments towards the predestined target area [42-44].

Presently, there are two different types of arc-based frame systems, arc-centered and target-centered, Figure 2. Arc-centered frames always have the target in the center of the arc, independent of the angle settings (For example: Leksell®

[2] MRI and CT are currently the only imaging methods for functional neurosurgery.

coordinate frame model G, Elekta Instrument AB, Sweden), while the target-centered frames can reach different target positions depending on the arc angles (For example: Brown-Robert-Wells BRW, Radionics Inc., USA). Normally, the frame is attached with four fixation screws directly to the skull under local anesthesia [44].

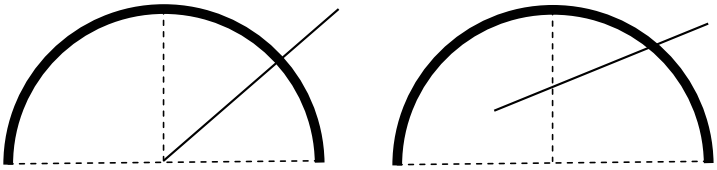

Figure 2. a) Arc centered principle, b) target centered principle.

Frameless systems in neurosurgery can be based on a passive robot arm with the surgical tool at the tip, or by a triangulating system using sound or light to keep track of the instrument in three dimensions. The principle behind all frameless systems is to keep track of the instrument position in relation to the target. Additionally, all stereotactic apparatus, both frame based and frameless systems, share one common principle; a coordinate translation is performed to relate the target position with the stereotactic coordinates. A frameless system is sometimes advantageous if a needed trajectory is located where the frame interferes with the instrument pathway, or if the patient's skull is too large for a frame to be mounted. However, when performing stereotactic and functional neurosurgery frame based systems are usually more common [45].

To find the anatomical landmarks and their relation to a stereotactic frame, an indicator system is used. Images visualizing both the brain and the indicator system simultaneously are recorded. When the anatomical landmarks are found in the images, the target coordinates are related to these landmarks using a stereotactic brain atlas [23]. The coordinates are finally translated to the stereotactic coordinate system.

An example of coordinate translation using the stereotactic frame and MR-indicator box from the Leksell Stereotactic System® (LSS, Elekta Instrument AB, Sweden) is presented in Figure 3. N-shaped fiducials[3] on the indicator box are visual on the acquired MR-images. The x and y coordinates of the target are calculated from the center of the image[4]. By measuring the distance between the corner fiducial and the oblique fiducial of the N-shaped indicator box markings, the Z-coordinate can be calculated in each image, Figure 3. The coordinate

[3] The fiducials in the LSS MR-compatible indicator-box consist of cupric sulphate solution, $CuSO_4$.
[4] The center is related to the corner fiducials of the indicator box.

translation of the target position from the images to the frame is calculated by, X = 100 ± x, Y = 100 ± y and Z = 40 ± z. From this, the coordinates X = 100, Y = 100 and Z = 100 always represent the center of the indicator box.

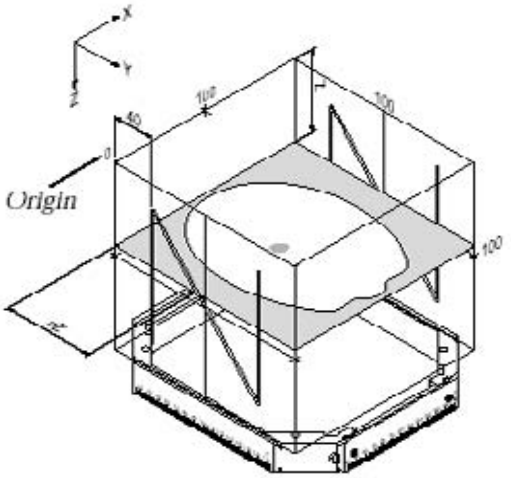

Figure 3. Coordinate system for the stereotactic frame (courtesy of Elekta).

2.2.2 Intracerebral guidance

Intracerebral guidance supports the surgeon with information that can be used for conclusions as to where the instrument is positioned. Principally, intracerebral guidance could be performed, either using intraoperative imaging methods or by direct measurements of the tissue type or neural response at the instrument tip during surgery. Different types of intracerebral guidance are chosen, depending on the surgery to be performed and depending on the surgeon's experience.

The time aspect during surgery is important, the patient is normally awake during these types of surgery and adding time-consuming guidance measurements should be avoided. Typically from the patient's point of view, the preparations before surgery, imaging and target calculations occupy 2-4 hours. The surgical DBS implant procedure takes 1-2 hours. After this, the battery pack and electrical leads are implanted and postoperative imaging takes several hours. Therefore, it is important to keep the intracerebral guidance time as short as possible. Presently, intracerebral guidance can last from minutes to several hours, depending on guidance method [46].

Navigation systems based on intraoperative imaging, have the advantage of delivering more or less real-time images while the surgical instrument is in place. For this purpose, methods of intraoperative MRI and CT as well as

ultrasound devices have been evaluated [47, 48]. The intraoperative MRI method is currently expensive and has low image resolution, especially for stereotactic and functional neurosurgery. Furthermore, the neurosurgical instruments have to be constructed of low-magnetic materials. Intraoperative MRI systems are typically based on an open 0.5 Tesla magnet, resulting in relative low resolution for functional neurosurgery (slice thickness[5] 5-7 mm) [48]. Intraoperative CT and ultrasound-based devices are still not applicable for clinical stereotactic and functional neurosurgery [47, 49]. Currently, image based navigation is primary used during tumor resection and other types of neurosurgical procedures.

Another type of navigation commonly referred to as neuronavigation [50], merges pre-surgical images with a tracking device placed on the surgical instrument. By this method, the instrument coordinates can be displayed in the pre-surgical images. These neuronavigation systems are hybrids between real-time positioning and pre-surgery imaging, not taking into account possible brain shift or the true location of the instrument inside the brain.

The existing intracerebral guidance methods based on measurements and stimulation of the brain tissue are: microelectrode and semi microelectrode recording [51], impedance measurements [46], microelectrode and macroelectrode stimulation [52, 53] as well as different optical methods [10, 54]. Of these methods, microelectrode recording together with impedance measurements and macrostimulation are the most commonly used methods today [7].

Microelectrode recording (MER) and semi microelectrode recording uses 1-5 sharp needles inserted into the target area (tip sizes in the µm scale). The needles record the firing pattern of a few neurons in a small volume [51, 55]. The target can then be plausible identified, usually by examining the time-sequence[6] of the different signals. Research is ongoing to improve the signal analysis in MER signals [56, 57].

When performing microstimulation and macrostimulation, a small stimulation current achieves a sensory or motor sensation in the patient, corresponding to the specific position. By mapping these responses from the patient, the desired target could be revised and a more accurate surgery could be performed. Microstimulation could use the same electrodes as for MER investigations.

[5] Slice thickness and image resolution is always a trade off against imaging time, the longer sequence time the higher resolution.
[6] The surgeon usually listens to the firing pattern of the neurons on a speaker in the operating theater, where gray matter has a higher neural activity than white matter.

Impedance measurements, using an RF-electrode tip is a common method for intracerebral guidance [52, 58]. The method originates from the discovery that white and gray brain tissue have different electrical conductivity [59, 60]. The sought target, commonly surrounded by white structures, could be identified via the differences in impedance. The impedance measurement represents a mean-value for the unisolated electrode tip, in contact with the tissue (usually 2-4 mm in length when using RF-lesioning electrodes). This results in a lower spatial resolution compared to the MER method [46].

There is an ongoing debate on hemorrhage risks when using intracerebral guidance methods [61]. Smoothly rounded electrodes have a lower hemorrhage risk and the needle-like MER electrodes have an increased risk. There are reports pointing to an elevated risk with smaller electrodes [61] and reports stating that no increased risk exists [51]. The available methods for target positioning during surgery present inconclusive results.

Optical methods for intra cerebral navigation have been proposed numerous times [10, 54]. Today there are research systems for developing these techniques. Near infrared spectroscopy [62], and the estimation of optical properties [63] are examples applied for the development of intracerebral guidance methods. The major advantage of using optical methods is the possibility to extract additional tissue information not previously available to the surgeon, and by this improve the intracerebral guidance. The basic idea is to investigate differences in optical properties between white and gray matter. This information is then used for mapping the target position in relation to surrounding structures. Moreover, optical measurements can be performed rapidly during surgery with instruments adapted for fiber optics, prolonging the procedure minimally [9, 10].

2.2.3 Radio frequency lesioning

During radio frequency lesioning [5], impedance measurements and macro stimulation are commonly used as intracerebral guidance complements. By this, different electrode localizations could be investigated before an irreversible RF-lesion is created.

RF-lesioning is based on a RF-electrode placed in the target area. The electrode tip is unisolated, and an alternating current is delivered to the tissue. To avoid stimulation of nerve cells during the lesion process, the alternating current has a high frequency[7]. During lesioning, the delivered current causes joule heating of

[7] Typically 512 kHz when using the RF-system from Elekta Instrument AB, Sweden.

the brain tissue, surrounding the RF-electrode. The current density is largest close to the RF-electrode tip, subsequently the temperature maximum is found outside, close to the tip [64]. A thermocouple in the RF-electrode tip is used for monitoring the tissue temperature. From this the delivered output effect can be controlled. When the tissue temperature rises above approximately 60 °C, the lesion begins, resulting in the destruction of the target neurons. After the commonly used 60 seconds of lesioning, the growth is stabilized.

2.2.4 Deep brain stimulation

During deep brain stimulation, a small flexible DBS-electrode[8] is stereotactically placed inside the target area, Figure 4. The implanted electrode is connected to a pulse generator, usually placed below the skin close to the clavicula. The DBS-electrode transmits short current pulses into the target, between the contact surfaces on the electrode or between the electrode and the pulse generator [65]. An example of an initial setting is an amplitude of 3-5 V using 60 µs pulse width at 130 Hz [66]. To achieve an effective suppression of the symptoms having minimal side effects, the initial settings are usually adjusted during postoperative follow-up [66].

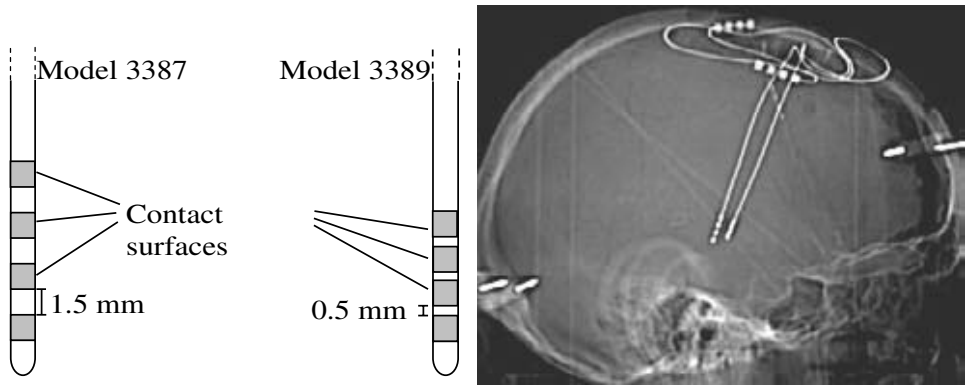

Figure 4. Example of two different DBS-electrodes (Medtronic Inc, USA). a) Schematic overview, b) CT image covering the two implanted DBS-electrodes.

The reversible nature of the DBS method is an advantage and the field of use is growing rapidly. However, there have been reports of depressions, speech deficits and other psychological effects during DBS [67, 68]. The DBS method is preferable for a large number of patients, but radio frequency lesioning still has its place among the neurosurgical methods arsenal [4, 69].

[8]The DBS electrode sizes are typically 1.27 mm in diameter and 9-12 mm long.

3 Biomedical optics background

The research in biomedical optics, both theoretical and applied, covers a wide range of theory and applications. Only the basic principles for the understanding of this thesis work will be addressed here.

Principally, photons can be both scattered and absorbed when injected into a turbid media such as the brain. Two basic processes describe the absorption of light. The carried energy can elevate the electron energy state in atoms, or it can result in increased vibrational and rotational states of molecules, usually known as heat [70].

Scattering events are usually characterized as elastic, quasi-elastic and inelastic. The principal differences between them are the energy transfer and possible frequency shift. An elastic scattering process conserves both energy and frequency of the scattered photon. Quasi-elastic scattering is prevailing for the Doppler effect, the scattering is elastic but becomes frequency shifted [70]. Inelastic scattering is an uncommon scattering type where the photon loses (or gain) energy during the process.

The absorption coefficient (μ_a), the scattering coefficient (μ_s) and the anisotropy factor (g), can characterize the optical properties of a tissue volume. The μ_a and μ_s parameters relate to the concentration and type of absorbers and scatterers in the tissue. The anisotropy factor g is defined as the statistical probability for a certain deflection angle at each scattering event, defined as the averaged cosine of the deflection angle ($-1 \leq g \leq 1$). For an anisotropy factor close to 1, the prevailing scattering will be deflected forward, while for a value close to 0 the scattering can occur in any directions, so called isotropic scattering. The optical properties of tissue are wavelength dependent. Hence, diverse wavelengths will be absorbed and scattered differently.

When estimating optical properties different combinations of μ_s and g values sometimes yield the same measured results. This is common when using diffuse reflectance methods. This effect is known as the similarity principle, and for two different optical properties it can be defined as $\mu_{s1}(1-g_1) = \mu_{s2}(1-g_2)$. The reduced scattering coefficient is therefore used, defined as a single parameter $\mu'_s = \mu_s(1-$

g). The relation $1/\mu'_s$ describes the reduced mean free path length of random walk in a media. In the same manner the mean free path lengths for scattering and absorption are defined as $1/\mu_s$ and $1/\mu_a$. The mean free path lengths describe the average step size each photon will travel before being scattered or absorbed.

The reduced scattering μ'_s incorporates both the anisotropy factor and the scattering and thereby influences the sampling volume. For a media with low scattering properties, the photons will have a larger sampling depth, while in a highly scattering media, the majority of the photons will be scattered around at a close distance from the injection point.

A fundamental equation in biomedical optics is the classical Lambert-Beers law Equation 1, describing the relation between the exponential attenuation of light in relation to the traveled distance. The original light intensity is denoted as I_0, the absorption coefficient μ_a, the distance d and the detected light intensity is denoted I.

$$I = I_0 e^{-(\mu_a)d} \tag{1}$$

The assumption for Lambert-Beers law is that no scattering events occur, only absorption. The analogous form in a medium containing only scatterers can be derived by replacing μ_a with μ_s in Equation 1. In media containing both absorbers and scatterers, the modified Lambert-Beers law describes the attenuation, Equation 2.

$$I = I_0 e^{-(\mu_a + \mu_s)d} \tag{2}$$

From Equations 1 and 2, the above Lambert-Beers law, the intensity of light that has been traveling in a turbid medium depends on both the scattering and absorption properties and thereby also on the wavelength. When injecting light into a tissue volume, the exponential decay of the injected light according to Equation 2 makes the sampled volume difficult to estimate. The majority of the light will be scattered and absorbed close to the injection point, while fewer photons will travel longer distances in the tissue volume.

In brain tissue, a variety of absorbers and scatterers exist. All molecules with refraction index mismatch will affect the scattering, mitochondria, lipids and blood cells are examples of scatterers. Water, oxygenated and deoxygenated hemoglobin (Hb and HbO_2) and lipids are the most common and well investigated chromophores [71]. An example of the wavelength dependent absorbance for different common chromophores can be seen in Figure 5. This

figure is compiled from data from the literature and presents water, Hb and HbO_2 and mammalian fat [72-74].

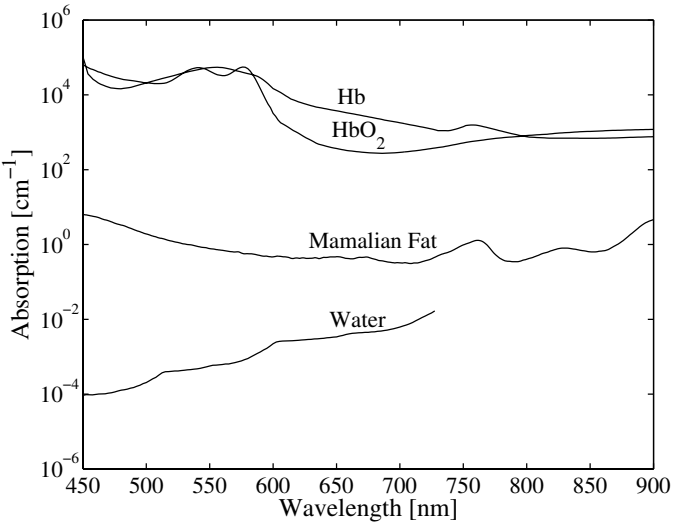

Figure 5. Compiled absorbance data from Hb, HbO_2, mammalian fat and water in the range of 450-900 nm.

In Figure 5, the typical double peak of HbO_2 at 542 and 577 nm and the Hb single peak at 555 nm can be seen. The differences in blood characteristic absorbance for Hb and HbO_2 at different[9] wavelengths are used in other optical techniques for measuring blood oxygenation level [75]. The absorption in water and fat is relative low compared to the absorption in blood, Figure 5. Additionally, fat in an extracted form, is a low absorber [71].

Optical properties derived from brain tissue, especially *in vivo*, are uncommon. A small collection of optical properties *in vivo,* and *in vitro*, from the human brain and *in vitro* from porcine brain is presented here, Table 1.

[9] The absorption differences at 660 or 940 nm and the isosbestic point at 804 nm are commonly used for estimating oxygenation.

Author/Tissue type	Wavelength (λ) [nm]	Absorption (μ_a) [cm^{-1}]	Reduced scattering (μ_s') [cm^{-1}]	Anisotropy (g) [a.u.]
Human brain				
White matter, *in vitro* Beek 1997 [76]	633	2.2	91	0.82
Gray matter, *in vitro* Beek 1997 [76]	633	2.7	20.6	0.9
White matter, *in vivo* Bevilacqua 1999 [77]	674	2.5	13.5	
Cortex matter, *in vivo* Bevilacqua 1999 [77]	674	0.2	10	
White matter *in vitro* Yaroslavsky 2002 [6]	630	0.8	65	0.86
Gray matter *in vitro* Yaroslavsky 2002 [6]	630	0.2	9.9	0.89
White matter *in vitro* Gottshalk 1992 [78]	630	1.5	54	0.86
Gray matter *in vitro* Gottshalk 1992 [78]	630	1.4	33	0.93
Porcine brain *in vitro*				
"brain" matter Wilson 1986 [79]	633	0.26	57	0.945
White matter[10]	633	2	100	0.74
Lesioned "brain" Matter[10]	633	3	65	0.74

Table 1. Example of optical properties in brain tissue, both porcine and human.

The differences in optical properties found in the literature are large, Table 1. Difficulties in estimating optical properties of brain tissue are plentiful. The estimated optical properties depend on the measurement equipment, test setup, choice of calculation model, and tissue preparation as well as the tissue temperature [80]. In addition, the brain in-homogeneity is a problem. White and gray tissues are difficult to separate visually and are often interwoven in the samples.

[10] Data from Paper V in this thesis.

3.1 Principles of laser Doppler perfusion monitoring

Laser Doppler flowmetry (LDF) is an established method to estimate the microcirculatory perfusion in a small tissue volume, mainly estimating the perfusion in capillaries, arterioles and venules. The principal definition of LDF perfusion values is the mean concentration of moving red blood cells multiplied by their mean velocity within the illuminated volume. The calculated perfusion values are relative and expressed as arbitrary units (a.u.).

In 1975, the first *in vivo* measurements of the skin microcirculation in humans were conducted, using coherent light scattering [81]. The LDF field was later divided into the Laser Doppler Perfusion Imaging (LDPI) [82] for non-touch mapping of superficial blood flow and Laser Doppler Perfusion Monitoring (LDPM) for measurements via fiber optics [83]. The application areas are many and includes measurements on the skin [84], heart [85] and brain [86].

As light can be described as waves, the superposition and frequency shift of light waves are the starting point in LDPM. When illuminating a tissue volume, containing a network of microvascular capillaries and a static supporting matrix, the backscattered light will become attenuated according to the Lambert-Beers law, Equation 2. A small fraction of the detected backscattered light will be frequency shifted[11] according to the Doppler principle. The maximal frequency shift Δf can be derived from the speed of the particle v and the light wavelength in the tissue λ, Equation 3 [87].

$$\Delta f = \frac{2v}{\lambda} \tag{3}$$

The magnitude of the frequency shift in LDPM investigations (for capillary flow of 1 mm/s in biological tissue) is typically in the range of a few kHz. Presented as wavelength this will be 10^{-18} m, while the laser frequency is approximately 10^{-7} m. This meaning that the frequency shift of photons is extremely small compared to the wavelength, and therefore impossible to detect using traditional spectroscopy methods. The collected photons both un-shifted and frequency shifted are instead detected using a photodetector. On the detector surface, the superposition principle of waves is the physics behind the formed speckle pattern, actually constructive and destructive interference between the mixed photons. Due to the moving red blood cells in the illuminated volume will the frequency shifts change and a stochastic fluctuating speckle pattern will arise.

[11] From the elastic and quasi-elastic scattering behavior of light in turbid media containing moving scatterers.

Usually two photodetectors are placed side by side and by illuminating both detectors simultaneously a differentiated detection can be derived to suppress common mode noise [83]. The photocurrent from the detectors is subtracted and the resulting signal contains the stochastic behavior of the signal. The resulting photocurrent includes both frequency and intensity information of the speckle pattern.

After low-pass and band-pass filtering of the differentiated electric current from the photodetectors two signals are extracted, the total backscattered light intensity (TLi[12]) and the stochastic fluctuating photodetector signal (AC). According to the LDF theory, the perfusion signal is calculated by the integrated power spectral density of the AC signal divided with the squared TLi signal, Equation 4 [87].

$$\text{Perfusion} = \frac{\int_{\omega_1}^{\omega_2} \omega P_{AC}(\omega) d\omega}{TLi^2} - f_{Noise}(TLi) \qquad (4)$$

In Equation 4, $P_{AC}(\omega)$ is the power spectral density of the photocurrent, AC signal. The function $f_{Noise}(TLi)$ is a linear noise function depending on the amount of light impinging the detector. ω_1 and ω_2 are the lower and upper cut-off frequencies typically 0.02 and 12 kHz in LDPM systems.

The calculated perfusion values are valid under the assumption of low fraction of moving red blood cells in the measured volume (actually a low degree of Doppler shifted photons). High concentration of moving scatterers result in high degree of shifted photons and multiple frequency shifts. This results in a non-linearity[13] behavior of the estimated perfusion values. For a high degree of multiple frequency shifts, the perfusion value will become underestimated.

[12] The nomenclature DC or TLi was used in the papers, both describing the total backscattered light intensity signal.

[13] The photodetectors and system bandwidth is usually not sufficient and thereby will energy at higher frequencies be lost.

Sources of errors and noise

A common error source during LDPM investigations is movement artifacts [88]. When the static tissue matrix moves the photons become Doppler shifted on both the moving red blood cells and the assumed static tissue. From this, the power spectrum ($P_{AC}(\omega)$ in Equation 4) will be broadened, with an overestimation of the perfusion signal as a result. Movement artifacts can be a major problem and have to be taken into consideration during LDPM measurements. In a stereotactic environment, the probes are supported by a stereotactic frame, firmly mounted on the patient's head. Therefore, no large tissue movement is present.

Two types of noise in LDPM systems can be found, originating from optical phenomena and the electronics. Common-mode noise, originating from fibers and laser stability, are suppressed using the differential detection technique [83].

The majority of electrical noise in LDPM systems originates from the photodetectors, i.e. dark current and shot noise[14]. When the photodetectors deliver a small current even if no light is present, this is referred to as dark current. The physics behind this is spontaneous electron emissions in the detector when the thermal energy is sufficient to breach the potential barrier in the detector. The dark current noise increases exponentially with temperature [89], and depends on the choice of electrical equipment in the system. The shot noise on the other hand is linearly dependent on the impinging light intensity. A compensation of shot noise is calculated, as the noise correction function $f_{Noise}(TLi)$, Equation 4. Shot noise originates from the electric conversion of light to electrons in the photodetectors.

[14] There are several other types of noise, from the electrical components or from the layout of the electronics etc.

3.2 Principles of diffuse reflectance spectroscopy

The diffuse reflectance spectroscopy method uses a broadband light source to illuminate a tissue volume. The light will be absorbed and scattered wavelength dependently, according to the tissue content. A diffuse reflectance spectrum presents the detected intensity as a function of wavelength. Wavelengths approximately within 400-700 nm are detectable with the human eye and usually denoted as visual spectra, while the interval of 700-3000 nm refers to the near infrared and infrared regime. The therapeutic window is usually defined as the wavelength interval 600-1300 nm, where the absorption in biological tissue is relatively low (mainly due to the low absorption of blood and water within this region).

Reflectance spectroscopy methods have been used since 1939. In the early era, they were used for studies of skin color [90]. The development of spectroscopy methods and instruments includes both invasive and non-invasive techniques. Diffuse reflectance spectroscopy measurements of white and gray human brain tissue have been performed *in vitro* [91, 92] and *in vivo* [9]. Studies of optical properties of lesioned and native human and porcine brain tissue *in vitro* have been reported [6, 93]. Estimation of tissue oxygenation level is a large field of non-invasive spectroscopic methods [94].

When illuminating a tissue volume, containing multiple types of chromophores, the recorded spectra is a combination of the properties from all underlying chromophores. Additionally, the concentration and type of scatterers vastly affect the spectral shape. The total superimposed effect of different chromophores is a major challenge when interpreting spectroscopic data, especially for measurements in living tissue. The best fit between a tissue measurement and the sum of several weighted experimentally derived chromophore spectra, could estimate the percentage of each identified chromophore in the tissue volume.

A diffuse reflectance spectrum contains information about the measured chromophores and scatterers as well as information of the system characteristics (light source, spectrometer detection efficiency and the probe characteristics). Each time the system is demounted, the system characteristics may change slightly. To minimize the system influence, normalization with a white calibration reference can be performed. The reference material is usually barium sulfate in a flat shaped disc, which has approximately 98 % reflectivity in the visual wavelength interval. Principally in diffuse reflectance spectroscopy investigations, a reflectance spectra $R(\lambda)$, is calculated by dividing the tissue measurement with a white calibration reference, while, the absorbance is calculated as the inverse logarithmic form of the reflectance $A(\lambda) = -\log(R(\lambda))$.

Light penetrating a tissue volume will be attenuated according to the Lambert-Beer law, Equation 2. In a small tissue example, containing only two different absorbers, the intensity of the detected light I, can be described as an exponential function, Equation 5.

$$I = I_0\left(e^{-(\mu_{a1})d} * e^{-(\mu_{a2})d} \right) = I_0 e^{-(\mu_{a1}+\mu_{a2})d} \tag{5}$$

A practical consideration, if the light source drifts is that during measurements the measured calibration is not representative to the conditions during the tissue measurements. By using a dual channel spectrometer, the light source can be recorded simultaneously as the tissue measurements. By this setup, a possible spectral drift in the lamp is detected and compensated for. The principal calibration normalization is described in Equation 6.

$$R(\lambda) = \underbrace{\frac{M_T(\lambda)}{M_{TL}(\lambda)}}_{\text{Tissue}} * \underbrace{\frac{1}{\left[\frac{M_C(\lambda)}{M_{CL}(\lambda)}\right]}}_{\text{Calibration}} \tag{6}$$

In Equation 6, $M_T(\lambda)$ and $M_C(\lambda)$ is the tissue and calibration measurements respectively, while $M_{TL}(\lambda)$ and $M_{CL}(\lambda)$ is the light source spectra during the tissue and calibration measurements. The calibration measurements are averaged to one single spectrum, corresponding to the system specific characteristics at the present measurement situation. In some situations, if a non-perfect reference standard was used, a correction can be calculated according to Equation 7.

$$R(\lambda) = \underbrace{\frac{M_T(\lambda)}{M_{TL}(\lambda)}}_{\text{Tissue}} * \underbrace{\frac{1}{\left[\frac{M_C(\lambda)}{M_{CL}(\lambda)}\right]}}_{\text{Calibration}} * \underbrace{\frac{\left[\frac{M'_C(\lambda)}{M'_{CL}(\lambda)}\right]}{\left[\frac{M'_W(\lambda)}{M'_{WL}(\lambda)}\right]}}_{\text{Correction}} \tag{7}$$

Principally, Equation 7 is an extension of Equation 6 multiplied with the correction factor, this transforms the used calibration measurement $M_C(\lambda)$ to a true white reference. More precisely, $M'_C(\lambda)$ is a spectrum measured on the used calibration material and $M'_W(\lambda)$ is a measurement on an accurate white reference. $M'_{CL}(\lambda)$ and $M'_{WL}(\lambda)$ are the corresponding light source spectra.

Sources of error and noise

In spectroscopy methods, error sources mostly originate from interfering background light and dark current influences. Usually, the experiment setup should handle background light problems. The physics behind dark current has been described in the chapter entitled *Principles of laser Doppler perfusion monitoring*. In spectroscopy, the dark current phenomenon can be corrected by subtracting a dark measurement according to Equation 8. The dark measurement is a blank measurement without any light impinging the detectors. In some spectroscopy systems, the internal design handles the dark current problems by subtracting these measurements automatically.

$$R(\lambda) = \frac{M_T(\lambda) - \text{dark}}{M_C(\lambda) - \text{dark}} \tag{8}$$

4 Aim of the thesis

The overall aims of this thesis were to study the development and to estimate the final size of RF-lesions using laser Doppler perfusion monitoring and to explore the possibility of developing an intracerebral guidance method based on diffuse reflectance spectroscopy. From these overall aims the following specific aims were formulated:

- To develop and evaluate a laser Doppler perfusion monitoring system suitable for the detection of lesion growth during stereotactic RF-lesioning.
- To study the time course of perfusion and total backscattered light intensity signals during *in vitro* and *in vivo* RF-lesioning, and to relate these signal changes to coagulation size.
- To explore the reflectance spectral characteristics of white, gray and lesioned porcine brain matter *in vivo*, as well as the optical properties of *ex vivo* porcine brain tissue.
- To investigate the spectral differences between white and gray matter as well as between white matter and functional targets in humans.

5 Equipment and validation

In this thesis work, two laser Doppler perfusion monitoring systems and two diffuse reflectance spectroscopy systems were used. In Figure 6, a schematic overview of the complete systems is displayed. All subsystems in the figure are further explained in the following sections of this chapter.

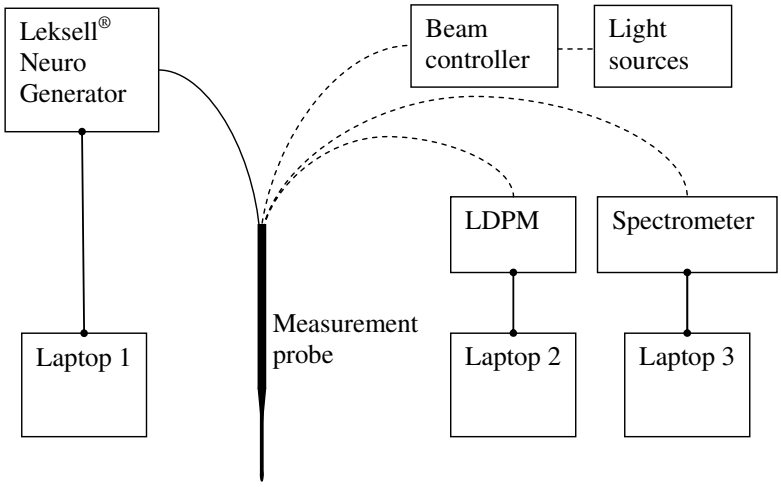

Figure 6. Schematic overview of the experimental systems in use during this thesis work.

5.1 Neurosurgical equipment

All stereotactic equipments in this thesis are parts of the Leksell® Stereotactic System (LSS, Elekta Instrument AB, Sweden). The lesions both *in vitro* and *in vivo* (Papers I, II and III), were created using a modified Leksell® Neuro Generator (LNG, Model 30-1, Elekta Instrument AB, Sweden). The LNG was modified to deliver a timestamp, in order to keep track of the lesioning time sequence, in relation to the acquired LDPM measurements. The LNG delivers a current frequency of 512 kHz and adjusts the power output based on temperature readings from a thermocouple in the electrode tip. The maximal temperature increase rate of the LNG is 6 °C/s, in order to reduce the risk of overheating the target with boiling as a consequence. The timestamps, impedance, delivered

output power and RF-electrode tip temperature were stored for post-processing in the performed studies.

A Leksell coordinate frame (model G, Elekta Instrument AB, Sweden) with modified posts, Figure 7 a), was used in the animal experiments (Papers II and III). The corresponding MR compatible indicator box (Elekta Instrument AB, Sweden) was used for the imaging procedures. The two anterior posts were replaced with two L-shaped modified posts [95], for better attachment to the porcine skull. As a comparison, the standard frame for human use is demonstrated in Figure 7 b). In addition, a specially designed punch for harvesting the lesioned brain tissue was used in Paper V. The punch and the modified posts are fully described elsewhere [95].

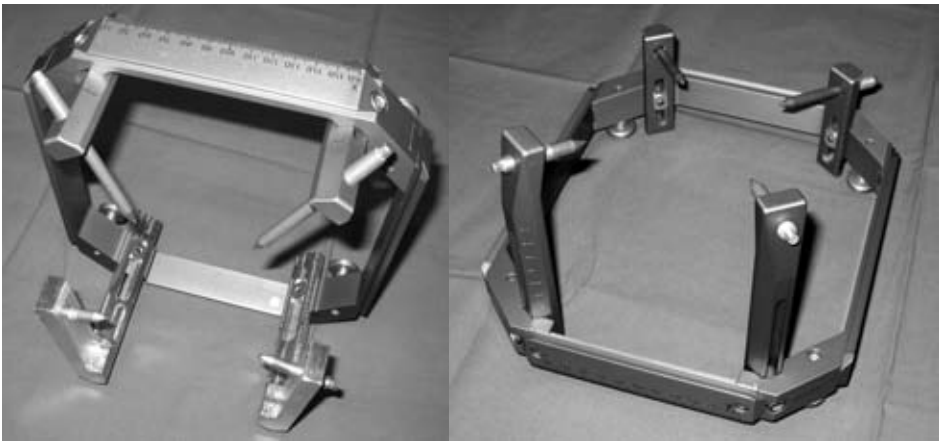

Figure 7. Example of the modification on the stereotactic frame. a) Modified posts for the porcine skull, b) unmodified human frame.

In Figure 7 b), the frame coordinate system is displayed. The origo of the frames coordinate system is located outside the indicator box at the patient's upper back right corner (superior lateral and posterior to the frame of the patient's right side). The x-axis points towards the patient's left side, the y-axis points forward and the z-axis points downward. This was important to note during the animal experiments. When mounting the frame on humans, they are usually sitting upright and the frame is placed as a crown on top of the head, Figure 8 b).

However, the animals were positioned on their abdomen, facing forward with the nose passing through the modified frame. By this, the coordinate system was flipped 90º forward around the x-axis. The origo was then located to the upper right corner in front of the animal's head, Figure 8 a).

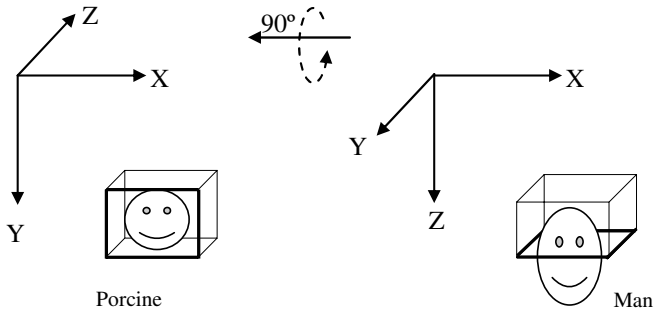

Figure 8. Coordinate system differences when mounting the stereotactic frame. a) Porcine skull and b) humans.

In summary, the attachment of the frame and animal position flipped the captured images two ways, 90º forward and 180º around the z-axis depending on the animal position during imaging. After imaging, both the Leksell SurgiPlan® (Elekta Instrument AB, Sweden) and Framelink™ Stealth station (Medtronics Inc, USA) have been used for surgery planning in the human study, Paper IV.

5.2 RF-electrodes and measurement probe

Three different probes were used, one standard monopolar RF-electrode from the Leksell® Stereotactic System as reference, and two specially designed fiberoptical probes. The developed measurement probes were constructed to fit into the coordinate frame model G, having a functional length of 190 mm and a shaft diameter of 2.2 mm. They were equipped with separate optical fibers for delivering and collecting light and had a smoothly rounded tip to minimize the trauma during probe insertion.

5.2.1 The angular RF-electrode

An angular RF-electrode following the same construction principles and dimensions as a standard monopolar RF-electrode was built. The electrode had an un-isolated tip length of 4 mm and a tip diameter of 2.2 mm. By incorporating a thermocouple inside the tip, the RF-electrode could be used for lesioning. A bundle (n = 18) of 240 µm multi-mode step-index[15] glass fibers was inserted along the electrode shaft. A conical mirror inside the tip dispersed the light perpendicular into, and collected light from, the investigated tissue via a transparent insulation. The angular RF-electrode could send and collect light in four different angles (one measurement direction at a time), Figure 9. Each measurement quadrant could be connected, either to an LDPM unit, or to a diffuse reflectance spectroscopy system. During the laboratory experiments in Paper I, only one measurement quadrant was in use for the LDPM measurements, while during the animal experiments in Papers II and III, three quadrants were used for LDPM and the fourth quadrant was connected to a spectrometer.

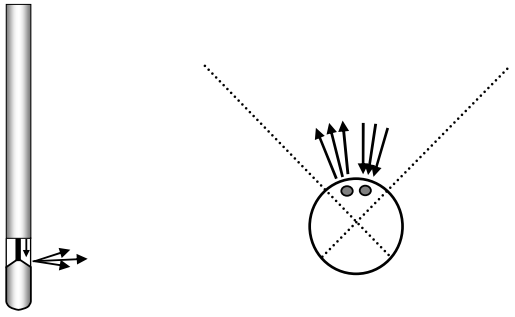

Figure 9. The angular RF-electrode and the principle of dispersing light, together with the view of the optical window seen from above, displaying the delivering and collecting of light in one measurement quadrant.

[15] Step index refers to fibers with a large difference of refractive index between the core and cladding.

5.2.2 The optical probe

An optical probe for human use without RF-lesioning and impedance measurement capacity was developed. In this probe, four optical fibers were directed out from the probe tip, in a forward direction. Two fibers were arranged for LDPM and two for spectroscopy measurements. By this setup, a small tissue volume in front of the probe was sampled. To minimize the probe and still have a rigid electrode, the probe diameter was reduced to 1.5 mm at the tip, while being 2.2 mm at the shaft. The design with fibers in front of the probe, stresses the demands on the tip shape. Meaning that the fully rounded shape was not possible and the tips were flat on top of the fiber ends. However, the rest of the probe tip was rounded. This developed probe was used for the diffuse reflectance spectroscopy measurements in Paper IV.

5.2.3 Electrode evaluation

To evaluate the lesioning capacity of the angular RF-electrode, a previously developed transparent homogeneous albumin solution was used [96]. The test solution consisted of 30 w/w % bovine albumin protein in saline (0.9 %) solution. The albumin solution mimics the lesion process in living brain matter [95, 97]. To estimate the coagulated sizes, a video system based on two perpendicular images was applied. By using the RF-electrode shaft as a size reference in the images, the coagulation sizes could be estimated [96].

Previous publications [95], showed a strong correlation between coagulation size and electrode settings. By choosing the RF-electrode type, electrode size[16] and target temperature (70-90 °C), a large variety of sizes can be created. Coagulations in the albumin solution were created at the three different temperatures of 70, 80 and 90 ºC, for comparison of the lesioning capacity between a standard RF-electrode and the developed angular RF-electrode could be performed. The coagulation sizes in the albumin solution using the two RF-electrodes are presented in Table 2.

	Volume mm^3		**Length mm**		**Width mm**	
	Standard	**Angular**	**Standard**	**Angular**	**Standard**	**Angular**
70 °C	58.2±2.7	51.7±3.6	5.9±0.1	5.5±0.2	4.3±0.1	4.2±0.1
80 °C	89.6±4.0	90.2±4.9	7.0±0.1	6.7±0.2	4.9±0.1	5.0±0.1
90 °C	164.0±26.3	157.6±11.9	8.5±0.6	8.4±0.3	6.1±0.3	6.0±0.1

Table 2. Coagulation sizes (m ± sd) in albumin solution using the angular and a standard RF-electrode. Both electrodes were 2 mm monopolar RF-electrodes, n = 10 for each electrode and temperature setting, data from Paper I.

[16] RF-electrode sizes are usually 1 or 2 mm diameter 2-4 mm unisolated tip length (Elekta Instruments, Sweden)

When performing *in vitro* coagulations, the test solution should be heated to 37 °C. If a coagulation of 80 °C is initiated, the actual temperature increase in the LNG will become 80-37 = 43 °C. This originates from the assumption of the LNG that the tip temperature always is 37 °C, even when this is not the case. To maintain a stable temperature in the test solution, a temperature stabilizer was built. Two cubic shaped containers with water circulating in between them were used. The water was heated to 37 °C and thereby the albumin solution in the inner container could be kept at 37 °C during the experiments. However, it is possible to change the LNG safety settings of initial temperature setting in the laboratory. By this, coagulations can be performed in albumin solutions at room temperature. Due to practical reasons of heating a rotational flow model in Paper I, this feature was used.

5.3 Laser Doppler Perfusion monitoring systems

Two LDPM systems were developed for this thesis work, one single channel and one four channel system. In addition, a commercial LDPM system (Periflux PF 5000 housing a PF 5150 LDPM unit, Perimed, Sweden) was used in an additional study[17] not presented in this thesis [98]. The photocurrent from the developed LDPM systems signals was sampled using an A/D converter (Daq-pad 3070, National Instruments, USA). The sampling frequency depends on the LDPM system. Frequencies of 50 and 100 kHz were used, Papers I and II. The photocurrent was recorded by LabView® (National Instruments Inc., USA) and stored in a personal computer for post processing in Matlab® (Mathworks Inc., USA).

5.3.1 Single and four channel LDPM system

The single channel system consisted of a 1 mW, 632.8 nm HeNe laser, the angular RF-electrode and a dual photodetector with the associated electronics. The light intensity from the RF-electrode tip, delivered from this system was always less than 1 mW. Backscattered light, collected by the angular RF-electrode, was mediated via an optical fiber onto the two photodetectors. The two detectors were arranged as a differential setup, to suppress common mode noise. After band-pass filtering (0.02 – 12 kHz) and amplification of the photocurrent, two signals remained. One signal represented the total backscattered light intensity (TLi) and the other signal contained the frequency content of the beating speckle formations, impinging the photodetectors. To achieve a perfusion signal, post processing of the two signals was performed

[17] The LDPM study in human brain tissue was conducted on the same patient material as in Paper IV.

according to Equation 4. This single channel LDPM system was used in the *in vitro* study, Paper I.

A refined version of the single channel LPDM system used four fibers, connected to four separate detector cards. One HeNe laser source (11 mW, 632.8 nm) and the angular RF-electrode were used in the system. Each of the four detector cards used the same differentiated dual mounted photodetectors as described above to suppress common mode noise [83]. From these detector cards four intensity and four frequency signals were A/D converted and stored into the computer. A beam controller, containing two step-motors equipped with mirrors, directed the laser light into one delivering fiber, Figure 10. By this setup, the system could perform measurements in four separate directions[18]. The laser effect into the tissue at the electrode tip was below 2 mW. This four channel LDPM system was used for the animal experiment in Paper II.

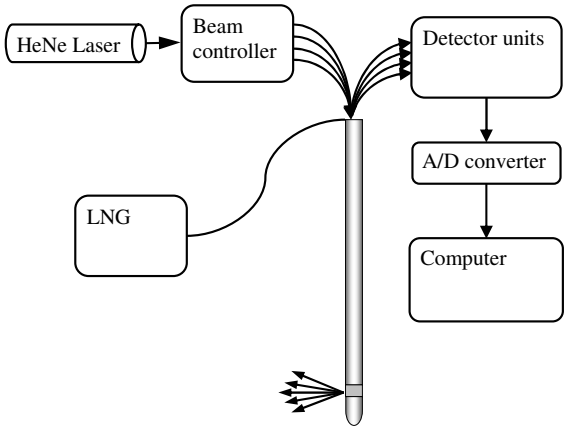

Figure 10. Four channel LDPM system overview.

[18] The angular RF-electrode made it possible to deliver light in one direction and calculate the perfusion in another, this increases the source-detection distance and possibly the sampling depth.

5.3.2 Laser Doppler system validation

To estimate the noise compensation values (primary shot noise), the detector surface was illuminated using a light emitting diode. The diode delivered light intensities corresponding to the full working range of the photodetector. From these measurements, a noise compensation function (f_{Noise} in Equation 4) was calculated for each detector card.

The LDPM system's linearity was evaluated using a standard flow model [88], consisting of a plastic tube (diameter = 1.5 mm) positioned in a piece of Delrin® plastic. The optical window of the angular RF-electrode was positioned perpendicular to the tube, Figure 11. A solution containing 1 part milk (3 % fat), and 100 parts of water was pumped through the tube having flow speeds ranging from 0 to 7 mm/s, using a syringe pump (M362, Sage™, Orion Research, Inc., USA). The developed systems were linear ($r = 0.99$, $p < 0.0005$, $n = 8$).

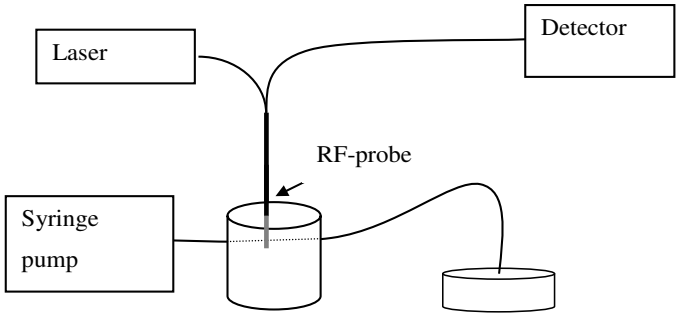

Figure 11. Test setup for linearity evaluation of the LDPM systems.

5.4 Diffuse reflectance spectroscopy systems

Both the angular RF-electrode and the optical probe were used in an animal and a human study. In the animal study (Paper III), the spectrometer AVS-MC2000 (Avantes, The Netherlands) and a halogen light source LS-1 (Ocean Optics, USA) were used, while in the human study (Paper IV), the AvaSpec-2048-5-RM spectrometer (Avantes, The Netherlands) and the light source HS 2000 (Top Sensor Systems, The Netherlands), were used. Both spectrometers had 2048 pixels CCD arrays and a resolution of approximately 1 nm within a wavelength interval of 400-900 nm.

In both spectrometers, two channels were used for detecting light. The first channel collected light from the tissue while the second channel measured the light directly from the light source. All measurements were recorded using LabView®. Routines for post processing of the collected spectra were developed in Matlab®. Equation 6 describes how to use a second channel of the spectroscope for compensating possible light source drift during measurements.

5.4.1 Spectroscopy system evaluation

The two commercial spectroscopy systems were evaluated by tests of the light source stability, the CCD array sensitivity and integration time linearity. The stability of the light sources was examined by a setup using a white reference. Measurements were captured every five minutes during two hours and thereby the stability was examined.

All spectrometers have different sensitivity of the CCD array. The sensitivity is strongly wavelength dependent in an individually different way for each channel. An example of the difference in sensitivity for a two-channel spectrometer can be seen in Figure 12. In the figure, a white reference tile (WS-2, Top Sensor Systems, The Netherlands) was measured using channels 1 and 2 (AvaSpec-2048-5-RM). The measurements in both channels were performed using the same probe and without changing any settings (distance between probe and reference tile and integration time).

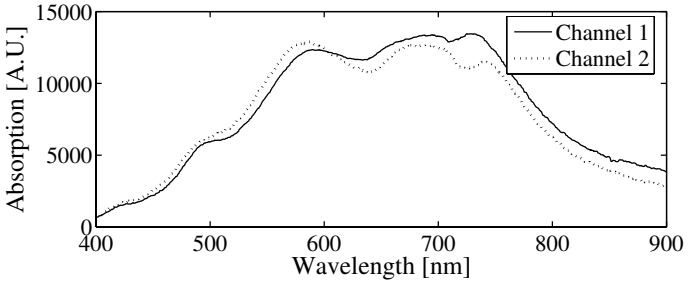

Figure 12. Light source and spectrometer characteristics for two separate channels.

The integration time linearity was tested by using different integration times during measurements on the reference tile. Measurements, using settings from 10 ms to 450 ms, covered the integration times applicable to the brain tissue experiments. A function corresponding to the system linearity was created by selecting the intensity at a chosen wavelength (700 nm) and plotting it against the integration time. An example from the linearity evaluation, using channel 1 in the AvaSpec-2048-5-RM system, is presented in Figure 13.

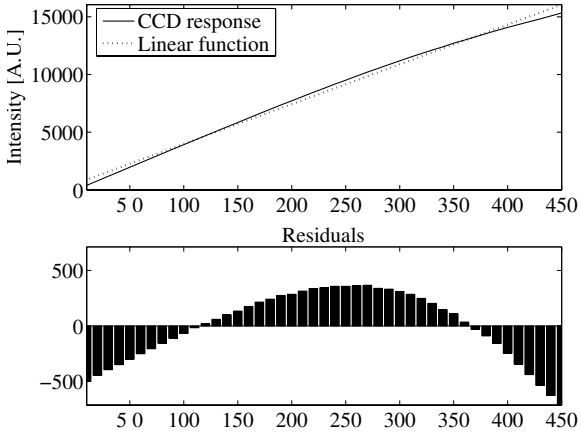

Figure 13. CCD array linearity measured at 700 nm plotted together with an estimated linear function (upper image). The corresponding residuals between the linear function and the measured linearity (lower image).

6 Experimental and surgical studies

This thesis is based on five different experimental studies, ranging from laboratory studies via animal experiments to measurements in the human brain during stereotactic and functional neurosurgery. Two principally different topics were addressed, the lesion size and development during RF-lesioning, and whether reflectance spectroscopy is suitable to use in brain tissue for a guidance purpose.

6.1 Laser Doppler perfusion monitoring during RF-lesioning

In brain tissue, the high capillary density together with the richness of slightly larger vessels such as arterioles and venules should result in a strong perfusion signal from an LDPM system. During RF-lesioning, the brain matter coagulates which results in vanishing blood flow and changes in optical properties. From this, a decrease in perfusion signal and changes in the total backscattered light intensity (TLi) should be possible to detect. Additionally, an increasing distance between the electrode tip and lesion border, should also result in larger changes in the perfusion and TLi signals. From the above reasoning, two hypotheses were formulated:

"When brain tissue coagulates, the perfusion signal decreases and the backscattered light intensity signal changes; both these changes are markers for lesion size, detectable using LDPM measurements"

"The differences in LDPM signal levels before and after lesioning are correlated to the size, and an increased lesion size results in larger changes of the signals"

6.1.1 Albumin flow model with scatterers, Paper I

By adding scatterers (glass microspheres, diameter = 11 µm, Potters Ltd, USA) into an albumin solution, a perfusion situation could be mimicked. A bowl, placed on top of a rotating disc filled with the solution, simulated the expected blood flow around the RF-electrode tip, Figure 14 a). The angular RF-electrode was positioned at a fix distance from the bowl's rotational center, having the delivered light directed perpendicular to the flow. By changing the revolving speed of the bowl, flow speeds at the electrode tip between 0-9 mm/s were evaluated, Figure 14 b).

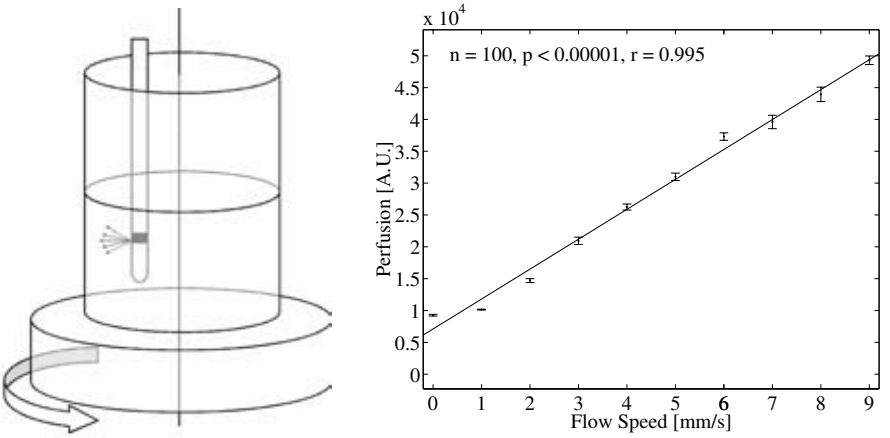

Figure 14. a) Rotating bowl flow model with scatterers. b) Linearity of the rotating albumin model.

The albumin model was adjusted for a flow speed of 1 mm/s. The flow speed during coagulation was experimentally decided, and is comparable to capillary flows in the human brain [11].

Coagulations using target temperatures of 70, 80 and 90 ºC (n = 10 for each temperature setting) were created. An example of both total backscattered light intensity and perfusion signals during coagulation in the rotational flow model using the three different temperatures is presented in Figure 15. In this study, the total backscattered light intensity was denoted DC, while in the thesis it is denoted TLi.

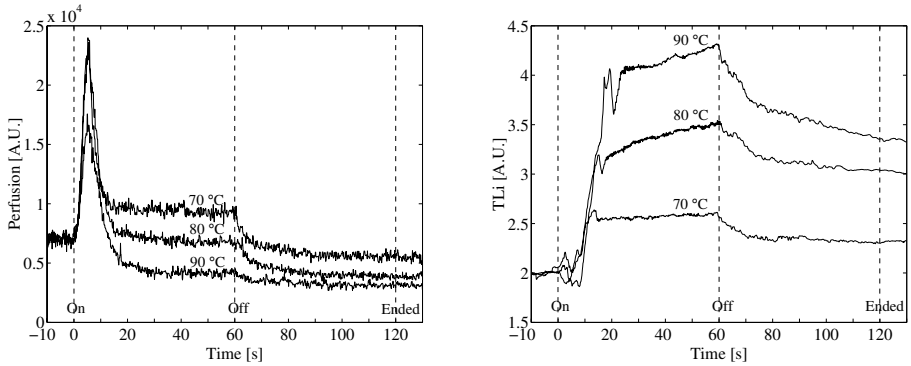

Figure 15. Example of signal changes during RF-lesioning at 70, 80 and 90º C *in vitro*. a) Perfusion signal changes, b) backscattered light intensity.

The albumin solution was relatively transparent, resulting in increasing TLi signals after coagulation. The coagulated albumin was denser with higher backscattered light intensity. In Figure 15 b), the change in TLi signals after coagulation corresponds to the different temperatures. The same principal behavior can be seen in the perfusion signal. Higher temperatures (larger coagulations) result in more pronounced differences in the perfusion signals. In Figure 15 a), the high perfusion peak is a result of increasing convective movements in the solution [97]. This peak starts to drop when the coagulation grows on top of the transparent window of the angular RF-electrode.

To test the hypotheses, the changes in LDPM signals before and after RF-lesioning at different temperatures were evaluated and the correlation between the coagulation sizes and the changes in LDPM signals were calculated.

6.1.2 RF-lesioning in porcine brain, Paper II

By using a previously developed protocol for stereotactic neurosurgery in the porcine brain [95], LDPM measurements were acquired during bilateral lesioning in living porcine brain tissue. The local ethical committee for animal research (D no.: 42-01, Linköping, Sweden) approved these animal experiments. The modified stereotactic frame was mounted on the pig skull during general anesthesia. Both T1 and T2 weighted MR-images of the porcine brain with the indicator box were recorded. An anatomical atlas of the porcine brain [99], together with the acquired MR-images were used by a neuroradiologist to identify two targets in the central gray matter. The selected targets corresponded to a bilateral thalamotomy in humans.

After trepanation of the skull and opening the dura, the angular RF-electrode was gently pushed into the brain tissue. LDPM measurements in three different directions were collected using incremental steps of 5 and 10 mm. In the target area, LDPM measurements were recorded before, during and after lesioning at different temperatures (70, 80 and 90 ºC, where n = 2, 6 and 4 respectively). The 80 ºC lesion was always performed in the left side in each porcine brain, while the temperatures on the right side were altered between 70 or 90 ºC.

A mean value of the signals 10 seconds before and 10 seconds after each lesion was calculated. The quotas between the mean valued signals, post/pre lesioning were used as one value in the following statistical analysis. In total 328 measurements were recorded in the 6 pigs, and 18 measurements were deleted due to high noise levels.

For lesion size estimation and electrode position verification, additional MR-images were captured after surgery. At the end of each experiment, the animals were sacrificed by an overdose of barbiturates intravenously and intracardially. Within approximately two hours, the lesioned tissue volume was stereotactically extracted. The removed tissue samples were placed in a freezer (-20 ºC) for later investigation (Paper V). An example of a 45° oblique T2 weighted MR-image after RF-lesioning can be seen in Figure 16.

Figure 16. Example of bilateral lesions in porcine brain in a 45º oblique MR-image.

The electrode trajectories are clearly visible in the MR-image, as well as the bilateral lesioned tissue volume, Figure 16. By counting the number of voxels covering the lesioned volume in the recorded MR-images and multiplying with the scale factor (1.06*1.06*3), the lesion size was estimated in mm^3.
A neuroradiologist examined the MR-images and classified the tissue types as white or gray matter at the measured positions along the electrode trajectory and in the target. The neuroradiologist's tissue classification was matched to the collected TLi signal behavior. The measurements in the target area were finally organized in two groups using both the TLi signal behavior and the neuroradiologist's tissue classification.

To test the stated hypotheses, the changes in LDPM signals during RF-lesioning were investigated. Furthermore the lesion size prediction capacity of the LDPM signals was evaluated, by comparing the signal changes to the different sized lesions.

6.1.3 Statistical tests and results, laser Doppler perfusion monitoring studies

From the RF-lesioning studies, the angular RF-electrode could create lesions and simultaneously measure both the perfusion and TLi signals. The signals were recorded during *in vitro* albumin experiments and during stereotactic and functional neurosurgery in porcine brain. The lesion sizes and corresponding standard deviations within one temperature setting were small, implying good reproducibility. The coagulation sizes were estimated via the video system for the albumin study, Table 2, and via MRI for the animal study. Lesion sizes of 116 mm^3 (70 ºC, n = 2), 227 mm^3 (80 ºC n = 6) and 299 mm^3 (90 ºC, n = 4), were estimated via MRI.

In the flow model study (Paper I), the changes in the perfusion and total light intensity were evaluated. While in the animal study (Paper II), these LDPM signals originated from two tissue groups. The intensity and perfusion signal changes for the two tissue types were denoted TLiA, TLiB, PerfA and PerfB[19].

In Figure 17, the changes in both perfusion and total light intensity signal changes are presented as a function of mean sizes of the coagulated albumin, recorded in the flow model. In the image, the scale on the y-axis is the relative signal changes before and after coagulation, calculated as Post/Pre. The scale on the x-axis is the temperature setting or the estimated coagulation size at the used temperatures (70, 80 and 90 ºC).

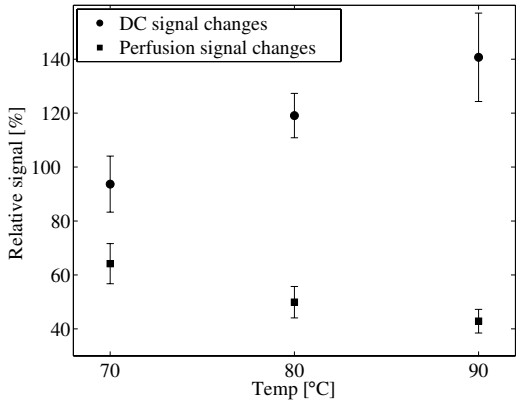

Figure 17. LDPM signal changes during RF-lesioning in albumin (n = 10 in each group).

In Figure 18, both perfusion and total light intensity signal changes during RF-lesioning in porcine brain are displayed. The two tissue types (corresponding to white and gray matter) are presented as a function of temperature. In Figure 18, the perfusion signal always decreases after lesioning while the TLi signal displayed a slightly increasing or decreasing behavior, depending on the measured tissue type.

[19] A corresponds to measurements in white matter, while B corresponds to gray matter.

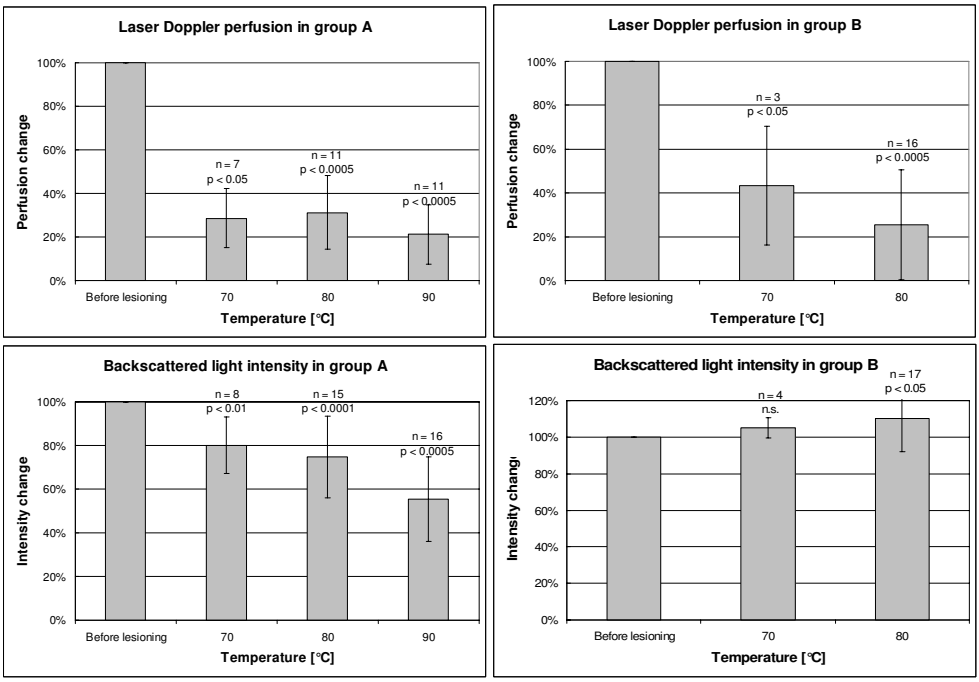

Figure 18. Perfusion and backscattered light intensity changes during RF-lesioning in porcine brain, measured in white and gray matter, group A and B respectively.[20]

[20] In group B, representing the TLi value at 80 °C, the real p-value was 0.5. This was overlooked during the printing of paper II.

Statistical tests
The first null hypothesis stated: "*There are no significant changes in the perfusion or intensity signal after lesioning*". The second null hypothesis stated: "*Larger lesions are not represented by significantly larger signal changes*".

The first null hypothesis was tested at the significance level of 0.05, using a paired two-tailed Student t-test in the flow model and a Wilcoxon two-sided matched-pair rank test in the animal study. The signals in the animal study did not fulfill the normal distribution criteria and therefore the Wilcoxon test was more proper to use.

The first null hypothesis was rejected at the significance level $p < 0.05$, for the flow model study when tested on the perfusion and intensity signal changes. In the animal study, the null hypothesis for the perfusion signals PerfA and PerfB was rejected at the significance level, $p < 0.05$. However, the intensity signal changes were only significant for the TLiA group. Additionally, the data in this study were grouped after the TLi signal behavior meaning that the statistical significance for TLiA is unreliable. Hence, only the perfusion signal changes are considered significant in both studies.

The second null hypothesis was tested by investigating the perfusion and intensity signal variations between different sized lesions in the two studies. There was modest violation against the normal distribution criteria for a traditional ANOVA design and therefore a Kruskal-Wallis test was used. The second null hypothesis was rejected at $p < 0.0005$ in the flow model for both the intensity and perfusion signal, meaning that there are significant differences in the signal changes when altering the coagulation size. However, in the animal study, only the TLiA signal was significant between 70-90 and 80-90 ºC lesions. As mentioned above, the data were grouped after this signal behavior and therefore the null hypothesis could not be rejected.

In addition, in the albumin flow model, the linear regression was calculated, describing the correlation between the coagulation size and TLi signal, ($r = 0.88$, $p < 0.0001$) and for the perfusion signal ($r = 0.81$ at $p < 0.0001$).

6.2 Diffuse reflectance spectroscopy experiments

White and gray matter has different optical properties, Table 1. This may be used for developing an intracerebral guidance method. By studying the spectral characteristics from diffuse reflectance spectroscopy measurements, it should be possible to separate white and gray matter. During lesioning, the optical properties are changing additionally and the same idea of separating native and lesioned brain tissue would therefore be achievable. From the above ideas, a hypothesis was formulated:

"*It is possible to differentiate between white and gray matter as well as lesioned brain tissue with diffuse reflectance spectroscopy measurements*"

6.2.1 Reflectance spectroscopy during RF-lesioning in porcine brain tissue, Paper III

All spectroscopy measurements in this study were collected during the same animal experiments as in Paper II. During the interventions, reflectance spectroscopy measurements along the electrode trajectory at incremental steps of 5 and 10 mm and in the target area before and after lesioning were acquired. At each measurement position, five consecutive spectra were collected and averaged. Before and after each measurement occasion, calibration measurements were performed. The wavelength interval in this study was 450-900 nm, using the spectrometer AVS-MC2000 and the halogen light source LS-1.

The angular RF-electrode design made it difficult to measure a white reference spectrum on a flat surface. To overcome this limitation, the white reference spectrum was instead calculated from three measurements using two probes. Two measurements were performed in a liquid motility standard (PF1001, Perimed AB, Sweden) using both the angular RF-electrode and a standard reflectance probe (FCR-14UV200-2-REF, Avantes, The Netherlands). The third measurement was performed on a flat reference tile using the same probe. The final white reference spectrum for the RF-electrode was then calculated according to Equation 9.

$$W(\lambda) = W_{Tile}(\lambda) - (M_{Av}(\lambda) - M_{RF}(\lambda)) \quad (9)$$

In Equation 9, $W(\lambda)$ denotes the calculated white reference spectrum for the angular RF-electrode. $M_{RF}(\lambda)$ and $M_{AV}(\lambda)$ represent the RF-electrode and standard probe spectra measured in the motility liquid. $W_{Tile}(\lambda)$ is the white reference tile spectrum measured with the standard probe.

The motility calibration measurements were captured before and after each porcine brain experiment. All calibration measurements were compared, in order to investigate if the light source drifted between experimental occasions. One calculated white reference spectrum was then used on all reflectance spectra in the study.

To test the stated hypothesis, all collected spectra were sorted from the neuroradiologist's tissue type classification and according to their spectral shape, into white or gray matter. A quotient of intensities at two different wavelengths (580 and 633 nm) was investigated for sorting the brain matter as white or gray. The same quotient was also investigated for discriminating between lesioned and native porcine brain matter.

When applying Equation 9, all spectra should be in logarithmic form. However, this was unfortunately overlooked and the correction is presented in Appendix.

6.2.2 Reflectance spectroscopy in human brain tissue during neurosurgery, Paper IV

During the human study, the optical probe was used together with the spectrometer AvaSpec-2048-5-RM and the light source HS 2000. All measurements were performed under local ethical permission (D. no.: M182-04) and all patients gave their informed consent. The study was a collaborational work with the Neurosurgical Departments at Linköping and Umeå University Hospitals. The patient material containing several different diagnoses is presented in Table 3. Unilateral or bilateral DBS implantation in patients suffering from movement disorders were performed during this study.

Targets	No. trajectories	Symptoms
STN	8	Parkinson, tremor
GPi	3	Dystonia
Zi	3	Tremor

Table 3. Targets and diagnoses for the patients operated on.

After pre-operative MR imaging and target coordinate calculations, a 14 mm burr hole was drilled and a durotomy performed. The optical probe was then gently pushed towards the target area. In total, 84 diffuse reflectance spectroscopy measurements were recorded at 40 or 30 mm above the target, and continued at the following positions 20, 10, 5, 2.5 mm and in the target.

The recorded spectra from different positions were classified as originating from white or gray matter, via the pre surgical MRI investigation or via the spectral shape in the recorded measurements. Two groups using different tissue type classifications were created, describing the tissue as white or gray matter. Additionally, cortex and functional targets were sorted respectively.

To remove all system influences on the measurements, spectra from white matter were divided with spectra from gray matter (within the same trajectory). The result is the difference spectra displaying the discrepancy between white and gray matter. All measurements in white and gray matter within the same trajectory were averaged respectively before divided. In total 8 difference spectra, between white and gray matter, were calculated using the MRI classification and 14 difference spectra using the spectral shape classification. Additionally, difference spectra between white matter and targets were calculated (7 spectra in STN, 3 spectra in GPi and 3 spectra in Zi).

Two different analysis methods were investigated in this paper. A simplified single wavelength analysis method was evaluated in relation to a previously developed slope algorithm [10] and the investigation of the differences between white and gray matter as well as between white matter and target tissue. The slope algorithm is based on fitting a linear equation to the recorded spectra in a wavelength interval, on unprocessed spectroscopy data. The tilt of the line is related to the tissue type, since white matter is more reflective than gray. The algorithm was applied on the acquired spectra (using the wavelength interval of 750-800 nm) together with calculating only the intensity at 780 nm. To compare the single wavelength analysis and the slope algorithm the correlation was calculated.

To test the stated hypothesis, the spectral differences between tissue types in the wavelength interval of 620-720 nm and at 780 nm were investigated. This was performed by calculating the averaged differences between the investigated tissue types.

6.2.3 Statistical tests and results, spectroscopy studies

The two spectroscopy studies, conducted in porcine and in human brain, differ from the perspective of statistical tests, these were only performed in the human study. The animal study was mainly performed to exemplify the idea of using spectroscopy methods for separating tissue types. However, statistical tests on the applied quotient analysis in Paper III were calculated after the original publication of the paper.

The averaged reflectance spectra from white and lesioned white matter in porcine brain are displayed in Figure 19 a), while the averaged reflectance spectra from gray and lesioned gray matter are displayed in Figure 19 b).

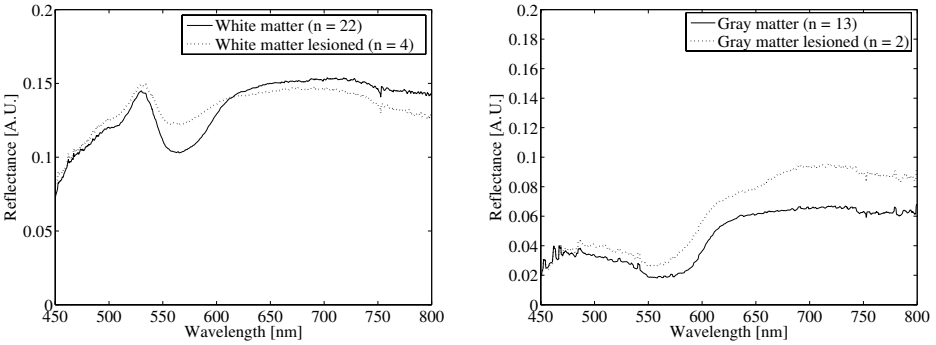

Figure 19. Averaged reflectance spectra recorded in porcine brain tissue. a) Lesioned and native white matter, b) lesioned and native gray matter.

The reflectance differences between averaged white and gray matter as well as between white matter and targets, recorded in human brain are shown in Figure 20.

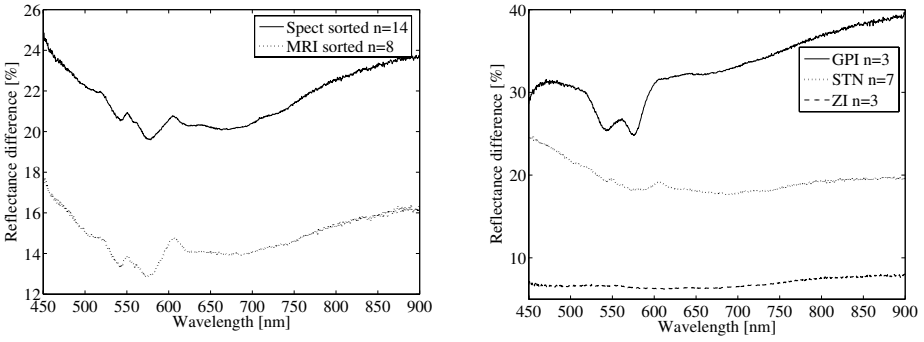

Figure 20. Averaged reflectance difference matter in human brain tissue. A) Between white and gray matter, b) between white matter and the targets of STN, GPi and Zi.

Statistical tests

The formulated null hypothesis, H_0: T*here are no significant spectral differences between white and gray matter*. This hypothesis was tested via a quotient analysis in the animal study (580 nm and 633 nm), and within a wavelength interval of 620-720 nm and a single wavelength of 780 nm in the human study.

The null hypothesis was tested using a Wilcoxon two-sided rank test in the animal study and a two-tailed student t-test in the human study. In the human study, the data fulfilled all requirements for a t-test. However, for the animal study, a small violation against the normal distribution constraint was present and therefore the Wilcoxon rank sum test was used.

In the animal study, the null hypothesis was rejected at $p < 0.005$ for the quotient value when tested between white and gray matter, at $p < 0.05$ between gray and lesioned gray matter. However, the null hypothesis could not be rejected for the test between white and lesioned white matter in the animal study. Due to the small number of spectra recorded in lesioned tissue ($n = 2$ and 4), the lesioned spectra should only be regarded as examples.

In the human study, the null hypothesis was rejected at $p < 0.05$ for all tested cases, Table 4.

MRI sorted $N_{trajectory} = 8$, $n_{white} = 15$, $n_{gray} = 22$			**Spectroscopy sorted** $N_{trajectory} = 14$, $n_{white} = 29$, $n_{gray} = 39$		
$m_{620\text{-}720}$ ± s.d. [%]	**m_{780} ± s.d. [%]**	**Slope analysis $m_{700\text{-}850}$ ± s.d. [a.u.]**	**$m_{620\text{-}720}$ ± s.d. [%]**	**m_{780} ± s.d. [%]**	**Slope analysis $m_{700\text{-}850}$ ± s.d. [a.u.]**
14 ± 13 $p < 0.05$	15 ± 13 $p < 0.05$	1.09 ± 2.02 Not significant	20 ± 6 $p < 0.0001$	22 ± 8 $p < 0.0001$	2.01 ± 2.18 $P < 0.01$

Table 4. Mean values (m ± s.d.) calculated from the difference spectra in the wavelength interval of 620-720nm and at 780 nm.

The group sorted after spectral shape includes several more spectra than the MRI classification still having a lower standard deviation, see Table 4. This indicates that spectroscopy measurements are more sensitive to tissue type than MRI.

The correlation between the tested slope algorithm and the single wavelength intensity was r = 0.99 (n = 84). Additionally, the tilt of a slope and the intensity value applied on unprocessed data displays principally the same information. Therefore, the tested slope algorithm could be replaced with the single wavelength at 780 nm in the human study.

6.3 Optical properties estimated from extracted porcine brain tissue, Paper V

From the porcine brain experiments in Papers II and III, tissue samples were extracted for determination of the optical properties, absorption and reduced scattering, μ_a and μ'_s. After the sacrification of the animal, the skull was opened and a cylinder shaped tissue sample was extracted. The samples were put in a -20 ºC freezer for storage. The cylinder shaped samples contained both the created lesion as well as native matter. After thawing, the samples were sliced and put between two glass sheets, using spacers of 0.3 mm thickness. Two groups, containing five white matter samples and five lesioned brain tissue samples were prepared and measured on, at room temperature.

A novel device for real-time measurements of optical properties has previously been developed at Lund University Medical Laser Center, the combined angular and spatial resolved head sensor (CASH). The device aims at being an alternative to the traditional integrating sphere (IS). The CASH sensor is based on a fiber optic setup and gives the possibility of measuring angular transmittance at two angles (α_0, α_1), reflectance (R) and transmittance (T), Figure 21. As light source, a steady state HeNe (2 mW, 633 nm) laser was used. If all parameters are measured simultaneously all three optical properties of μ_a, μ_s and g can be estimated.

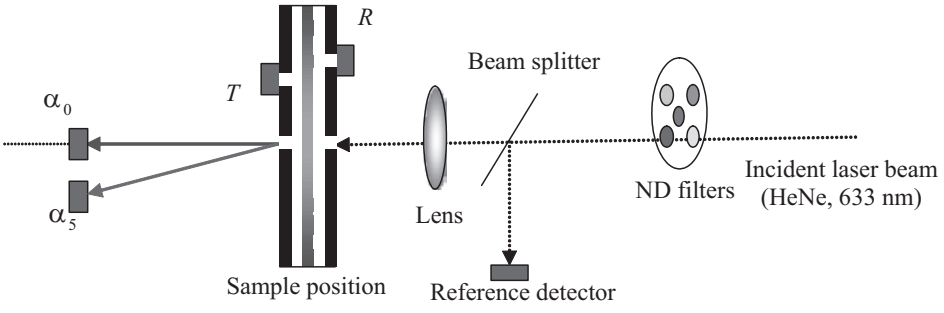

Figure 21. CASH sensor setup, reflectance R, transmittance T, angular transmittance at 0º and 5ºdenoted as α_0, α_1 respectively.

During this study a two-parameter setup was used, collecting only the reflectance R and transmittance α_0 from the CASH sensor, Figure 21. From this setup, the absorption and reduced scattering parameters μ_a and μ'_s, can be estimated. To estimate the same parameters using the integrating sphere setup, the total reflectance and total transmittance were measured.

A 75 W Xe lamp delivered the light for the integrating sphere measurements. The transmittance and reflectance measurements were collected simply by altering the side of the tissue sample on the integrating sphere. A nitrogen cooled CCD camera recorded the measurements. A deeper description of the integrating sphere and CASH sensor is described elsewhere [100, 101].

After the tissue sample measurements, an intralipid-ink calibration matrix (10*10 samples) covering the expected optical parameters, was measured with both the systems. Additionally, Monte-Carlo simulations using the same optical properties as the measured calibration matrix were calculated. The simulated and measured calibration data were used for the calibration and for solving the inverse problem.

A fifth degree multiple polynomial regression model was used for mapping the optical properties in relation to the measured tissue and calibration measurements. Reflectance and transmittance as a function of optical properties for the two systems $R_{IS}(\mu_a,\mu'_s)$, $T_{IS}(\mu_a,\mu'_s)$ and $R_{CASH}(\mu_a,\mu'_s)$, $\alpha_0(\mu_a,\mu'_s)$ for the integrating sphere and CASH sensor respectively. The best fit of the polynomial function for mapping the tissue measurement with the calibration matrix contains the optical parameters.

The CASH sensor was shown to be reproducible for measurements of intralipid-ink samples. The variations within tissue measurements when measuring at several different positions on the same sample were estimated. The variations for the absorption μ_a was 15 % and 17 %, for white and lesioned matter respectively. The variations for the reduced scattering μ'_s were 8 % and 4 %, for white and lesioned matter respectively. The estimated optical parameters, at the wavelength of 633 nm for the two systems are presented in Table 5.

	CASH [cm^{-1}]	**Integrating sphere [cm^{-1}]**
White matter, μ_a	2	2
Lesioned tissue, μ_a	3	3
White matter, μ'_s	100	70
Lesioned tissue, μ'_s	65	50

Table 5. Measured optical properties (cm^{-1}), using integrating sphere and CASH sensor.

7 Summary of papers

7.1 Paper I, Radio frequency electrode system for optical lesion size estimation in functional neurosurgery

The aim in this study was to investigate if LDPM measurements were possible to record during RF-lesioning, and if changes in the signals could be used as markers for coagulation size estimation. To evaluate this, an *in vitro* flow model, a monopolar RF-electrode with fiber optics and an LDPM system was developed. The developed RF-electrodes coagulation performance was equivalent to a standard RF-electrode of the same type and dimensions. An albumin protein solution, diluted with microspheres, was used in a rotating flow model for evaluating the signal changes during coagulation. Coagulations were performed at three different temperatures (70, 80 and 90 °C) to achieve different sized coagulations. In the flow model, both the perfusion and total backscattered light intensity signal changes were correlated to the created sizes. From this study, it was found that LDPM measurements were possible to record during RF-lesioning and the sizes can be estimated using optical markers *in vitro*.

7.2 Paper II, Optical measurements during experimental stereotactic radiofrequency lesioning

In this study, LDPM measurements were recorded in living porcine brain tissue during stereotactic RF-lesioning. The aim was to evaluate the developed LDPM system and angular RF-electrode *in vivo*, and to relate the LDPM signals to the developed lesion size. Six pigs were operated on in the central gray area, corresponding to a bilateral thalamotomy in humans. Measurements were performed at incremental steps towards the target, and in the target area. The optical properties in white and gray matter affect the behavior of the LDPM signals. Therefore, two groups of tissue types were identified from MRI and from the behavior of the total backscattered light intensity signal. From this study, it was found that the presence of a lesion could be detected by the perfusion signals. The time course of the lesion could also be followed by the LDPM signals. Additionally, the sampling volume of the system made the correlation between lesion sizes and signal changes difficult and only a trend could be detected.

7.3 Paper III, In vivo reflection spectroscopy measurements in pig brain during stereotactic surgery

The aim of this study was to explore the spectral characteristics of white and gray porcine brain matter, both native and lesioned. The developed angular RF-electrode was used for diffuse reflectance spectroscopy measurements in the wavelength interval of 450-800 nm. Recordings were collected at incremental steps along the trajectory towards the target area. In the target, measurements were recorded before and after RF-lesioning. The tissue at the recorded positions was classified as white or gray from both MRI and spectral shape. Differences in spectral characteristics were found between the investigated tissue types, both between white and gray matter and between native and lesioned matter. The differences in spectral characteristics between white and gray matter supports the idea of using optical techniques for developing a new intracerebral guidance method.

7.4 Paper IV, Diffuse reflectance spectroscopy measurements for tissue type discrimination during deep brain stimulation

In this study, an optical probe without lesioning capacity was developed for diffuse reflectance spectroscopy measurements in humans. The aim of this study was to investigate the spectral differences between white, gray and target tissue in the human brain during stereotactic neurosurgery, and to evaluate two different spectral analysis methods. Spectroscopy measurements were recorded at incremental steps towards and in different functional targets. The measurements were performed during DBS surgery in three different functional targets (STN, GPi and Zi). The recorded spectra were classified as white or gray using two different methods, via the preoperative MRI investigation or by sorting the data after spectral characteristics. The measurements were analyzed using the both tissue classification methods for comparison.

A previously developed slope analysis on unprocessed spectra was compared with a single wavelength analysis method. Both these analysis methods have comparable tissue discriminating capacity. In the study, significant intensity differences between white and gray matter were found. Spectral differences between white matter and functional targets were also identified.

7.5 Paper V, In vitro measurements of optical properties of porcine brain using a compact novel device

The aim of this study was to estimate optical properties in porcine brain tissue before and after RF-lesioning and to evaluate the possibility of accurate real tissue measurements from a developed instrument. The absorption μ_a and reduced scattering μ'_s coefficients were estimated in the study, while the anisotropy factor g was assumed constant. The paper describes the estimation of optical properties in tissue samples using two different techniques, integrating sphere measurements and combined angular and spatial resolved head sensor measurements. A batch of intralipid-ink solutions with different optical properties were used as the calibration matrix. Monte-Carlo simulations of the calibration matrix together with a multiple polynomial regression technique were the base for estimating the optical properties. The absorption and reduced scattering in white matter and in a mixed matter group of lesioned porcine brain tissue were presented.

8 General discussion and conclusions

RF-lesioning and intracerebral guidance during functional and stereotactic neurosurgery have been in focus for this thesis work, where the primary methodology was LDPM and diffuse reflectance spectroscopy measurements. The performed studies span from laboratory experiments via animal research to measurements in the human brain at clinical neurosurgery.

One underlying idea throughout this thesis was to explore the possibility of using one or two different wavelengths for tissue differentiation during surgery, still having the possibility of LDPM measurements. The quest for both lesion size estimation and the improvement in intracerebral guidance was the primary reason for the choice of using two different optical methods in this thesis. However, a controversy exists, for the lesion size estimation using LDPM a large sampling depth is preferable, while during intracerebral guidance a high spatial resolution is beneficial. In Papers I and II, LDPM measurements were performed using a 633 nm laser. Therefore, the wavelength of 633 nm was incorporated in the quotient analysis using reflectance spectroscopy in Paper III. In Paper IV, the analysis at the wavelength of 780 nm was chosen on the same premises. This wavelength corresponds to an LDPM study in the human brain in progress [98].

Tissue measurements were recorded with the constructed angular RF-electrode during lesioning. From the LDPM studies in Papers I and II, it was found that direct feedback of the lesion process could be presented to the surgeon. Up to now, the surgeons have to rely on postoperative MRI investigations of the created lesion. However, the angular RF-electrode had two major drawbacks, the reduced efficiency to deliver and collect light as well as the internal reflection. Numerous prototypes were designed and built in the effort to minimize these issues. The angular RF-electrode used in Papers I to III was sufficiently effective. From the experiences gathered in these studies, an optical probe was constructed and applied in the human measurements, in Paper IV. Additionally, a multipurpose RF-electrode has been developed for human use. This RF-electrode has the same optical setup as the optical probe together with RF-capacity. The multipurpose RF-electrode can record impedance,

temperature, spectroscopy and LDPM data, and future studies in humans are planned for evaluating this device.

The sampling depth strongly affects the results from the two optical technologies used in this thesis. The sampling depths for optical measurements are strongly dependent not only on the optical properties of the investigated tissue, but also on the used wavelength and probe geometry. Several authors have investigated the sampling depth by different models, including both phantom measurements and Monte Carlo simulations [102, 103]. Depending on the optical properties and model setup, penetration depths between 0.2 and 3 mm have been reported. The optical properties used as model input are however difficult to estimate, and this will directly affect the outcome of penetration depth in simulations. Previous studies have shown large variations (a factor of 10) in estimated optical properties of white and gray tissue, Table 1. Paper V in this thesis, exemplifies the diversity of optical properties, also when measured within the same sample. Differences in sampling position and in-homogeneity within each sample were probably the major reason for the discrepancies in optical properties.

During RF-lesioning, the maximal coagulation radius is approximately 2 mm measured from the electrode surface, when using a 2 mm in diameter monopolar RF-electrode at 90 ºC, Paper I and [96]. The lack of absorbers and the low concentration of scatterers in the albumin flow model, in Paper I, contributed to a large sampling depth. Therefore, the created lesion sizes could be correlated to the measured differences in LDPM signals. In brain tissue, the sampling depth is expected to be smaller. Additionally, the sampling depth in white matter is even smaller than in gray matter according to the literature [103]. From this, larger lesions were only detectable as a trend, not as statistically significant LDPM signal changes, sees Paper II. This is probably a result of the statistical investigation and the sampling depth of the system used. The statistical investigation was calculated on a small data set (number of lesions were 2, 4 and 6 for the three temperatures). Consequently, the low number of lesions in the study might have influenced the statistical results. The angular RF-electrodes internal reflection and the used wavelength of 633 nm also influence the sampling depth. Ways of increasing the sampling depth in the LDPM application could be to change the used light source to a longer wavelength and further develop the probe. Parts of these suggestions have already been implemented by the mentioned multipurpose probe together with a 780 nm LDPM unit.

In the animal experiments, both LDPM and spectroscopy measurements were recorded, see Papers II and III. The aimed targets were located in gray tissue, but due to the angular RF-electrodes design, the measurements were recorded perpendicular to the electrode, approximately 2 mm above the center of the lesion. The measurements were collected close to the border between white and gray matter or in some cases in white matter. This was a major reason for uncertainties in the differentiation of tissue types during these investigations. This was also why the definition, group A and group B was used, instead of white and gray matter, see Paper II. The total backscattered light intensity signal in Paper II, displays two distinct behaviors following RF-lesioning, increasing or decreasing, depending on tissue type. From Paper III, white tissue becomes darker and gray tissue becomes brighter as in Figure 19, during RF-lesioning in porcine brain. In analogy from Paper III, the group A in Figure 18 should therefore correspond to white matter and group B to gray matter.

The resolution of MRI investigations is lower than the spatial resolution of diffuse reflectance spectroscopy measurements [103]. A minor change in position of the measurement probe can result in large spectral variations of the signal, while still being within the same voxel in the MR-image. The MRI slice thickness was approximately 3 mm in the animal experiments, Papers II and III. In the human study, Paper IV, 2 mm slice thickness was used. In all studies, the pixel resolution was approximately 1 mm. One way of improving the resolution is by changing the MRI system. When using a 4.7 T MRI scanner instead of a 1.5 T scanner a tissue resolution from approximately 1 to 0.3 mm is achievable, using the same sequence [104]. The resolution in the used MRI systems and the difficulties to separate small areas of white and gray matter is major issues for tissue classification using MRI as reference. In addition, the electrode trajectories were tilted 45° in the animal experiments. Accordingly, the optical measurement site could be located in between voxels, which by definition reflects a mean value of the tissue.

All reflectance spectroscopy measurements were sorted into white or gray matter (and a mixed matter group, not used in the analysis) based on preoperatively T2-weighted MR-images, Papers III and IV. By using MRI as classification method of tissue type, a large uncertainty is introduced as mentioned above. To minimize this influence in Paper III, the spectra were first sorted from the neuroradiologist's MRI classification but the spectral shape was also taken into account. Due to experiences in Paper III, a more strict way of grouping the measurements was introduced in Paper IV. The measurements were sorted both after the spectral characteristics and the experience of the neurosurgeons in interpreting the MR images. This resulted in two groups representing each classification method. Hence, when computing an averaged

spectrum, displaying the characteristics of white or gray matter, the presented spectral shape might differ slightly, depending on how the spectra are sorted.

Only a few authors have evaluated diffuse reflectance spectroscopy in the human brain during stereotactic and functional neurosurgery [9, 10, 62]. Currently, the only proposed analysis method for discrimination of white and gray matter is to represent the tissue types with the tilt of a calculated slope, within the wavelength interval (700-850 nm) [10]. The proposed slope algorithm can probably be replaced by using a single wavelength as presented in Paper IV. Additionally in Paper IV, possible different spectral characteristics between functional targets were presented. The dataset in the study was small but the idea was presented. There is probably much more information within the recorded spectra, not addressed in Paper IV. Other analysis methods could present tissue oxygenation or the concentration of chromophores to the surgeon as guidance support [105]. Other possibilities are to estimate optical properties in vivo and relate these to intracerebral structures. Future studies should therefore aim at investigating if it is possible to differentiate functional targets using optical methods. If this ultimate goal is fulfilled, the possibility for a direct answer of target type in front of the electrode could revolutionize intracerebral guidance. It might replace the currently used microelectrode-recording standard.

As a conclusion of this thesis work, a laser Doppler perfusion monitoring system was developed for detecting coagulations during stereotactic RF-lesioning. The changes in laser Doppler perfusion monitoring signals were correlated to developed lesion size, *in vitro*, however the *in vivo* size estimation via LDPM signals in porcine brain could not be statistical verified. Further on, the spectral characteristics of porcine brain displayed large differences in reflectivity between white and gray matter, and different spectral characteristics between native and lesioned tissue. In human brain tissue significant differences between white and gray matter as well as between white matter and functional targets were found. In both studies, white matter displayed larger reflectivity than gray matter which supports the idea of developing an intracerebral guidance system.

Independent of which surgery type is performed; RF-lesioning or DBS implants, the results and summarized experiences presented in this thesis might be used for designing a measurement system for lesion size estimation and intracerebral guidance towards the target area.

9 Acknowledgements

I would especially like to thank my supervisor Professor Karin Wårdell, for continuously providing guidance and positive feedback. I would also like to thank Ola Eriksson, Ph.D. for his encouragement and support throughout this thesis work. Other important persons have been Håkan Rohman and Per Sveider for building all our fiber optic devices. I would also like to send great thanks to all coauthors in my publications Håkan Lindstam, M.D. and Peter Lundberg, Ph.D. for contributions in Paper II and III, Nazila Yavari, Ph.D. and Professor Stefan Andersson-Engels from the department of physics at Lund University for Paper V. In Paper IV, the neurosurgeons from Umeå University Hospital, Patric Blomstedt, M.D., Professor Marwan Hariz, and Professor Tommy Bergenheim, and the neurosurgeons from Linköping University Hospital, Johan Richter, M.D. and Peter Zsigmond M.D. made this paper possible.

I would also like to thank my colleagues at the Division of Biomedical Instrumentation (BIT) for general support, reading my material and giving me feedback, the rest of my colleagues at the department for providing a friendly and inspiring atmosphere. At the end of this thesis I would like to explain my sincear grattidude to my parents and to my both favorite sisters, I will never forget all support from you through my life. This thesis is dedicated to my family and especially to my beloved wife Anette, thank you for your endless support, understanding, never-ending patience with my sometimes strange ideas, for giving birth to our son Gabriel, and for carrying our expected baby. I love you all!

The Vinnova funded Swedish Competence Centre of Noninvasive Medical Measurements, NIMED supported this work.

10 Appendix

From Equation 9, the white reference spectra measured in the motility solution for both the angular RF-electrode and the standard probe ($M_{RF}(\lambda)$ and $M_{AV}(\lambda)$) are shown in Figure 22 a). The calculated white reference spectra for the RF-electrode and the white reference measured on the reference tile ($W(\lambda)$ and $W_{Tile}(\lambda)$) with the standard probe are shown in Figure 22 b).

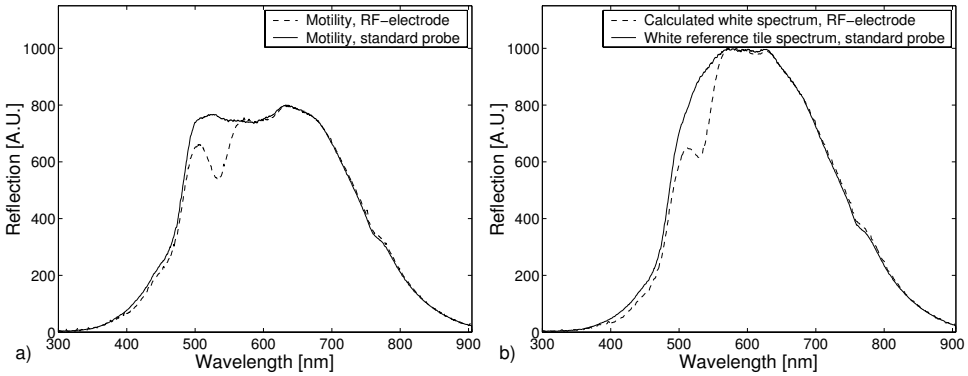

Figure 22. a) Measured white reference in motility liquid with the angular RF-electrode and the standard probe. b) Calculated white reference for the angular RF-electrode and measured white reference on a reference tile using the standard probe.

An error occurred in the calculation of the white reference spectra in Paper III, Equation 9. When applying the equation, each spectrum has to be in logarithmic form (absorption spectra are additive, not reflectance spectra). A corrected white reference spectra was calculated according to Equation 10.

$$W(\lambda) = \log(W_{Tile}(\lambda)) - (\log(M_{Av}(\lambda)) - \log(M_{RF}(\lambda))) \quad (10)$$

The corrected white reference spectra is plotted together with the original calculated white reference spectra, see Figure 23.

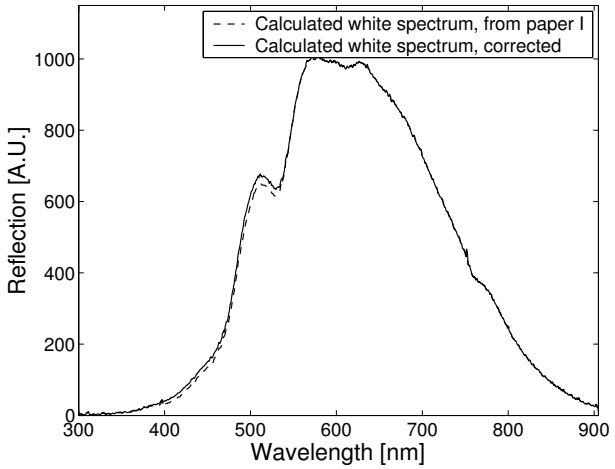

Figure 23. The calculated white reference spectra together with the corrected version, Paper III.

To investigate if the corrected white reference influenced the results from Paper III, the spectra were recalculated. In Figure 24, the spectra from white and gray matter are plotted together with the corrected white and gray matter spectra.

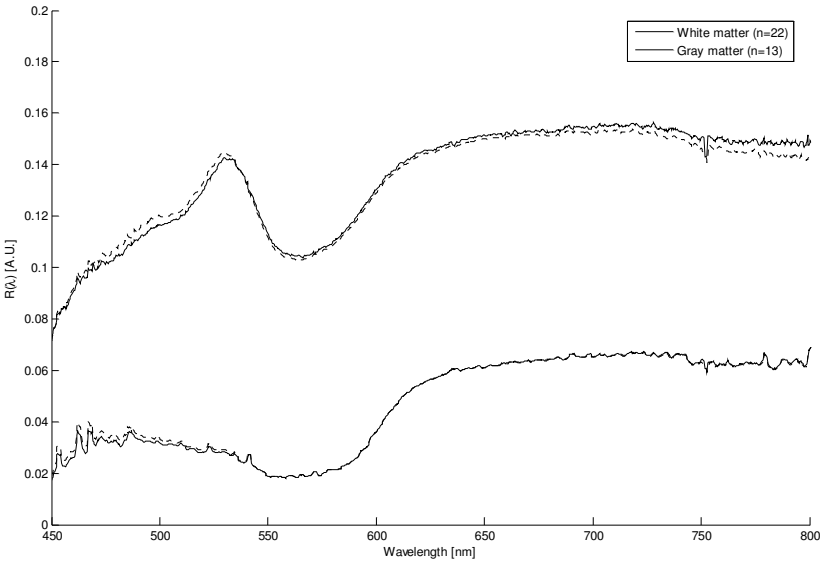

Figure 24. Averaged spectra from reflectance spectroscopy in porcine brain tissue, Paper III. Both original and corrected spectra, original represented by solid line and corrected represented by dotted line

11 References

1. Koller, W.C., Minagar, A., Lyons, K.E., and Pahwa, R., *Surgical treatment of Parkinson's disease*, in *Surgical treatment of Parkinson's disease and other movement disorders*, Tarsy, D., Vitek, J.L., and Lozano, A.M., Editors. 2003, Humana Press inc.: Totowa.
2. Spiegel, E.A. and Wycis, H.T., *Stereotaxic apparatus for operations on human brain.* Science, 1947. **106**: p. 349-350.
3. Leksell, L., *A stereotaxic apparatus for intracerebral surgery.* Acta Chirurgica Scandinavica, 1949. **99**: p. 229-233.
4. Laitinen, L.V., Bergenheim, A.T., and Hariz, M.I., *Leksell's posteroventral pallidotomy in the treatment of Parkinson's disease.* J Neurosurg, 1992. **76**(1): p. 53-61.
5. Benabid, A.L., Pollak, P., Gervason, C., Hoffmann, D., Gao, D.M., Hommel, M., Perret, J.E., and de Rougemont, J., *Long-term suppression of tremor by chronic stimulation of the ventral intermediate thalamic nucleus.* Lancet, 1991. **337**(8738): p. 403-6.
6. Yaroslavsky, A.N., Schulze, P.C., Yaroslavsky, I.V., Schober, R., Ulrich, F., and Schwarzmaier, H.J., *Optical properties of selected native and coagulated human brain tissues in vitro in the visible and near infrared spectral range.* Phys Med Biol, 2002. **47**: p. 2059-2073.
7. Rezai, A.R., Kopell, B.H., Gross, R.E., Vitek, J.L., Sharan, A.D., Limousin, P., and Benabid, A.L., *Deep brain stimulation for Parkinson's disease: surgical issues.* Mov Disord, 2006. **21 Suppl 14**: p. S197-218.
8. Winkler, D., Tittgemeyer, M., Schwarz, J., Preul, C., Strecker, K., and Meixensberger, J., *The first evaluation of brain shift during functional neurosurgery by deformation field analysis.* J Neurol Neurosurg Psychiatry, 2005. **76**(8): p. 1161-3.
9. Giller, C.A., Johns, M., and Liu, H.L., *Use of an intracranial near-infrared probe for localization during stereotactic surgery for movement disorders.* J Neurosurg, 2000. **93**: p. 498-505.
10. Johns, M., Giller, C.A., and Liu, H.L., *Computational and in vivo investigation of optical reflectance from human brain to assist neurosurgery.* Journal of Biomedical Optics, 1998. **3**(4): p. 437-445.
11. Tortora, G.J. and Grabowski, S.R., *Principles of Anatomy and Physiology*. Ninth ed. 2000: John Wiley & Sons, Inc.
12. Duck, A.F., *Physical properties of tissue*. 1990, Cambridge: The University Press.
13. Fillerup, D.L.a.M., J.F., *The lipids of the aging human brain,*. Lipids,, 1967. **2(4)**: p. pp295-298.
14. Nolte, J., *The human brain an introduction to its functional anatomy*. Fifth Edition ed. 2002: Mosby.

15. Helenius, J., Perkiö, J., Soinne, L., Østergaard, L., Carano, R.A.D., Salonen, O., Savolainen, S., Kaste, M., Aronen, H.J., and Tatlusimak, T., *Cerebral hemodynamics in a healthy population measured by dynamic susceptibility contrast MR imaging.* Acta Radiologica, 2003. **44**(5): p. 538-546.
16. Pantano, P., Baron, J.-C., Lebrun-Grandié, P., Duquesnoy, N., Bousser, M.-G., and Comar, D., *Regional cerebral blood flow and oxygen consumption in human aging.* Stroke, 1984. **15**(4): p. 635-641.
17. E Haug, O.S., V Sjaastad, *Människans Fysiologi*. 1992: Liber Utbildning AB.
18. Ma, T.P., *The Basal Nuclei*, in *Fundamental Neuroscience*, Haines, D.E., Editor. 2002, Churchill Livingstone: China. p. 405-422.
19. Wichmann, T. and Vitek, J.L., *Physiology of the basal ganglia and pathophysiology of movement disorders*, in *Surgical treatment of Parkinson's disease and other movement disorders*, Tarsy, D., Vitek, J.L., and Lozano, A.M., Editors. 2003, Humana Press inc.: Totowa.
20. Wichmann, T. and DeLong, M.R., *Models of basal ganglia function and pathophysiology of movement disorders.* Neurosurg Clin N Am, 1998. **9**(2): p. 223-36.
21. Atkinson, J.D., Collins, D.L., Bertrand, G., Peters, T.M., Pike, G.B., and Sadikot, A.F., *Optimal location of thalamotomy lesions for tremor associated with Parkinson disease: a probabilistic analysis based on postoperative magnetic resonance imaging and an integrated digital atlas.* J Neurosurg, 2002. **96**(5): p. 854-66.
22. Andy, O.J., *Thalamic stimulation for chronic pain.* Appl Neurophysiol, 1983. **46**(1-4): p. 116-23.
23. Niemann, K. and van Nieuwenhofen, I., *One atlas - three anatomies: relationships of the Schaltenbrand and Wahren microscopic data.* Acta Neurochir (Wien), 1999. **141**(10): p. 1025-38.
24. Midlöv, P., Eriksson, T., and Petersson, J., *Parkinsons sjukdom*, in *Läkemedelsboken*, AB, A., Editor. 2005, Apoteket AB: Stockholm.
25. Zhang, Z.-X., Roman, G.C., Hong, Z., Wu, C.-B., Qu, Q.-M., Huang, J.-B., Zhou, B., Geng, Z.-P., Wu, J.-X., Wen, H.-B., Zhao, H., and Zahner, G.E.P., *Parkinson's disease in China: prevalence in Beijing, Xian, and Shanghai.* The Lancet, 2005. **365**(9459): p. 595-597.
26. Tarsy, D., Vitek, J.L., and Lozano, A., *Surgical Treatment of Parkinsons's Disease and Other Movement Disorders*. Current Clinical Neurology, ed. Tarsy, D., Vitek, J.L., and Lozano, A. 2003: Humana Press.
27. Volkmann, J. and Sturm, V., *Pallidal deep brain stimulation for Parkinson's disease*, in *Surgical treatment of Parkinson's disease and other movement disorders*, Tarsy, D., Vitek, J.L., and Lozano, A.M., Editors. 2003, Humana Press inc.: Totowa.
28. Machado, A., Rezai, A.R., Kopell, B.H., Gross, R.E., Sharan, A.D., and Benabid, A.L., *Deep brain stimulation for Parkinson's disease: surgical technique and perioperative management.* Mov Disord, 2006. **21 Suppl 14**: p. S247-58.
29. Kitagawa, M., Murata, J., Uesugi, H., Kikuchi, S., Saito, H., Tashiro, K., and Sawamura, Y., *Two-year follow-up of chronic stimulation of the posterior subthalamic white matter for tremor-dominant Parkinson's disease.* Neurosurgery, 2005. **56**(2): p. 281-9; discussion 281-9.
30. Iskandar, B.J. and Nashold, B.S., Jr., *History of functional neurosurgery.* Neurosurg Clin N Am, 1995. **6**(1): p. 1-25.
31. Carlsson, A., *A paradigm shift in brain research.* Science, 2001. **294**(5544): p. 1021-4.
32. Kelly, P.J., *Stereotactic surgery: what is past is prologue.* Neurosurgery, 2000. **46**(1): p. 16-27.
33. Kelly, P.J., *Pallidotomy in Parkinson's disease.* Neurosurgery, 1995. **36**(6): p. 1154-7.

34. Benabid, A.L., *[History of stereotaxis].* Rev Neurol (Paris), 1999. **155**(10): p. 869-77.
35. Snyder, B.J. and Olanow, C.W., *Stem cell treatment for Parkinson's disease: an update for 2005.* Curr Opin Neurol, 2005. **18**(4): p. 376-85.
36. Okano, H., Yoshizaki, T., Shimazaki, T., and Sawamoto, K., *Isolation and transplantation of dopaminergic neurons and neural stem cells.* Parkinsonism Relat Disord, 2002. **9**(1): p. 23-8.
37. Björklund, A., Dunnett, S.B., Brundin, P., Stoessl, A.J., Freed, C.R., Breeze, R.E., Levivier, M., Peschanski, M., Studer, L., and Barker, R., *Neural transplantation for the treatment of Parkinson's disease.* Lancet Neurol, 2003. **2**(7): p. 437-45.
38. Rehncrona, S., *A critical review of the current status and possible developments in brain transplantation.* Adv Tech Stand Neurosurg, 1997. **23**: p. 3-46.
39. Freed, C.R., Greene, P.E., Breeze, R.E., Tsai, W.Y., DuMouchel, W., Kao, R., Dillon, S., Winfield, H., Culver, S., Trojanowski, J.Q., Eidelberg, D., and Fahn, S., *Transplantation of embryonic dopamine neurons for severe Parkinson's disease.* N Engl J Med, 2001. **344**(10): p. 710-9.
40. Redmond, D.E., Jr., *Cellular replacement therapy for Parkinson's disease--where we are today?* Neuroscientist, 2002. **8**(5): p. 457-88.
41. Horsley, V. and Clarke, R.H., *The structure and functions of the cerebellum examined by a new method.* Brain, 1908. **31**: p. 45-124.
42. Galloway, R.L., *Frameless stereotactic systems*, in *Textbook of Stereotactic and Functional Neurosurgery*, Tasker, G.a., Editor. 1996, Kingsport: Quebecor. p. 177-181.
43. Gabriel, E.M. and Nashold, B.S., Jr., *Historical development of stereotactic frames*, in *Textbook of Stereotactic and Functional Neurosurgery*, Tasker, G.a., Editor. 1996, Kingsport: Quebecor. p. 29-47.
44. Lunsford, L.D., Kondziolka, D., and Leksell, D., *The Leksell stereotactic system*, in *Textbook of Stereotactic and Functional Neurosurgery*, Tasker, G.a., Editor. 1996, Kingsport: Quebecor. p. 51-63.
45. Holloway, K.L., Gaede, S.E., Starr, P.A., Rosenow, J.M., Ramakrishnan, V., and Henderson, J.M., *Frameless stereotaxy using bone fiducial markers for deep brain stimulation.* J Neurosurg, 2005. **103**(3): p. 404-13.
46. Laitinen, L.V. and Hariz, M., *Movement Disorders*, in *Neurological Surgery*, Youmans, J., Editor. 1996, Saunders: Philadelphia. p. 3575-3609.
47. Broggi, G., Ferroli, P., Franzini, A., Dones, L., Marras, C., Marchetti, M., and Maccagnano, E., *CT-guided neurosurgery: preliminary experience.* Acta Neurochir Suppl, 2003. **85**: p. 101-4.
48. Mamata, Y., Mamata, H., Nabavi, A., Kacher, D.F., Pergolizzi, R.S., Jr., Schwartz, R.B., Kikinis, R., Jolesz, F.A., and Maier, S.E., *Intraoperative diffusion imaging on a 0.5 Tesla interventional scanner.* J Magn Reson Imaging, 2001. **13**(1): p. 115-9.
49. Unsgaard, G., Rygh, O.M., Selbekk, T., Muller, T.B., Kolstad, F., Lindseth, F., and Hernes, T.A., *Intra-operative 3D ultrasound in neurosurgery.* Acta Neurochir (Wien), 2006. **148**(3): p. 235-53; discussion 253.
50. Fontaine, D., Duffau, H., and Litrico, S., *[New surgical techniques for brain tumors].* Rev Neurol (Paris), 2006. **162**(8-9): p. 801-11.
51. Gross, R.E., Krack, P., Rodriguez-Oroz, M.C., Rezai, A.R., and Benabid, A.L., *Electrophysiological mapping for the implantation of deep brain stimulators for Parkinson's disease and tremor.* Mov Disord, 2006. **21 Suppl 14**: p. S259-83.
52. Shalit, M.N. and Mahler, Y., *Brain impedance measurements by the use of small bipolar needle electrodes.* J Appl Physiol, 1966. **21**(4): p. 1237-42.

53. Hobza, V., Jakubec, J., Nemeckova, J., Nemecek, S., and Sercl, M., *Impedance monitoring in the stereotactic localization of intracranial structures.* Sb Ved Pr Lek Fak Karlovy Univerzity Hradci Kralove, 1995. **38**(1): p. 33-46.
54. Jeon, S.W., Shure, M.A., Baker, K.B., Huang, D., Rollins, A.M., Chahlavi, A., and Rezai, A.R., *A feasibility study of optical coherence tomography for guiding deep brain probes.* J Neurosci Methods, 2006. **154**(1-2): p. 96-101.
55. Tasker, R.R., Yamashiro, K., Lenz, F., and Dostrovsky, J.O., *Thalamotomy for Parkinsons´s disease: Microelectrode technique.* Modern stereotactic neurosurgery, 1988: p. 297-314.
56. Falkenberg, J.H., McNames, J., Favre, J., and Burchiel, K.J., *Automatic analysis and visualization of microelectrode recording trajectories to the subthalamic nucleus: preliminary results.* Stereotact Funct Neurosurg, 2006. **84**(1): p. 35-44; discussion 44-5.
57. Falkenberg, J.H., McNames, J., and Burchiel, K.J., *Automatic microelectrode recording analysis and visualization of the globus pallidus interna and stereotactic trajectory.* Stereotact Funct Neurosurg, 2006. **84**(1): p. 28-34.
58. Laitinen, L., Johansson, G.G., and Sipponen, P., *Impedance and phase angle as a locating method in human stereotaxic surgery.* J Neurosurg, 1966. **25**(6): p. 628-633.
59. Latikka, J., Kuurne, T., and Eskola, H., *Conductivity of living intracranial tissues.* Physics in Medicine and Biology, 2001. **46**(6): p. 1611-1616.
60. Gabriel, S., Lau, R.W., and Gabriel, C., *The dielectric properties of biological tissues: II. Measurements in the frequency range 10 Hz to 20 GHz.* Phys Med Biol, 1996. **41**(11): p. 2251-69.
61. Hariz, M.I., *Safety and risk of microelectrode recording in surgery for movement disorders.* Stereotact Funct Neurosurg, 2002. **78**(3-4): p. 146-57.
62. Giller, C.A., Liu, H.L., Gurnani, P., Victor, S., Yasdani, U., and German, D.C., *Validation of a near-infrared probe for detection of thin intracranial white matter structures.* J Neurosurg, 2003. **98**: p. 1299-1306.
63. Johns, M., Giller, C.A., D., G., and Liu, H.L., *Determination of reduced scattering coefficient of biological tissue from a needle-like probe.* Optics Express, 2005. **13**(13): p. 4828-4842.
64. Wren, J., Eriksson, O., Wårdell, K., and Loyd, D., *Analysis of temperature measurement for monitoring radio-frequency brain lesioning.* Med Biol Eng Comput, 2001. **39**(2): p. 255-62.
65. Benabid, A.L., Pollak, P., Hoffmann, D., and Munari, C., *[Stimulators of the central nervous system].* Rev Prat, 1993. **43**(9): p. 1129-39.
66. Deuschl, G., Herzog, J., Kleiner-Fisman, G., Kubu, C., Lozano, A.M., Lyons, K.E., Rodriguez-Oroz, M.C., Tamma, F., Troster, A.I., Vitek, J.L., Volkmann, J., and Voon, V., *Deep brain stimulation: postoperative issues.* Mov Disord, 2006. **21 Suppl 14**: p. S219-37.
67. Anderson, K.E. and Mullins, J., *Behavioral changes associated with deep brain stimulation surgery for Parkinson's disease.* Current Neurology and Neuroscience Reports, 2003. **3**: p. 306-313.
68. Bejjani, B.P., Damier, P., Arnulf, I., Thivard, L., Bonnet, A.M., Dormont, D., Cornu, P., Pidoux, B., Samson, Y., and Agid, Y., *Transient acute depression induced by high-frequency deep-brain stimulation.* New England Journal of Medicine, 1999. **340**(19): p. 1476-1480.
69. Okun, M.S. and Vitek, J.L., *Lesion therapy for Parkinson's disease and other movement disorders: Update and controversies.* Movement Disorder, 2004. **19**(4): p. 375-389.

70. Tuchin, V., *Light-Tissue Interactions*. Biomedical photonics handbook, ed. Vo-Dinh, T. 2003: CRC press LLC.
71. Hollis, V., *Non-invasive monitoring of brain tissue temperature by near-infrared spectroscopy*, in *Department of Medical Physics and Bioengineering*. 2002, University College London: London.
72. van Veen R.L.P., S.H.J.C.M., Pifferi A., Torricelli A., Cubeddu R., *Determination of VIS- NIR absorption coefficients of mammalian fat, with time- and spatially resolved diffuse reflectance and transmission spectroscopy.* OSA Annual BIOMED Topical Meeting, 2004.
73. Zijlstra, W., Buursma, A., and Assendelft, O., *Visible and Near Infrared Absorption Spectra of Human and Animal Haemoglobin*. 2000: Brill Academic Publishers.
74. Pope M. Fry, E.S., *Absorption spectrum (380700nm) of pure water. II. Integrating cavity measurements.* Appl. Opt., 1997. **36**: p. 8710--8723.
75. Williams, I.M., Mortimer, A.J., and McCollum, C.N., *Recent developments in cerebral monitoring--near-infrared light spectroscopy. An overview.* Eur J Vasc Endovasc Surg, 1996. **12**(3): p. 263-71.
76. Beek, J.F., Blokland, P., Posthumus, P., Aalders, M., Pickering, J.W., Sterenborg, H.J., and van Gemert, M.J., *In vitro double-integrating-sphere optical properties of tissues between 630 and 1064 nm.* Phys Med Biol, 1997. **42**(11): p. 2255-61.
77. Bevilacqua, F., Piguet, D., Marquet, p., Gross, J.D., Tromberg, B.J., and Depeursinge, C., *In vivo local determination of tissue optical properties: applications to human brain.* Applied Optics, 1999. **38**(22): p. 4939-4950.
78. Gottschalk, W., *Ein Messverfahren zur Bestimmung der Optischen Parameter biologischer Gevebe in vitro*. 1992, Universitaet Fridriciana: Karlsruhe.
79. Wilson, B.C., Jeeves, W.P., and Lowe, D.M., *In vivo and post mortem measurements of the attenuation spectra of light in mammalian tissues.* Photochem Photobiol, 1985. **42**(2): p. 153-62.
80. Joel Mobley, T.V.-D., *Optical Properties of Tissue*. Biomedical photonics handbook, ed. Vo-Dinh, T. 2003: CRC press LLC.
81. Stern, M., *In vivo evaluation of microcirculation by coherent light scattering.* Nature, 1975. **254**: p. 56-58.
82. Wårdell, K., Jakobsson, A., and Nilsson, G., *Laser Doppler perfusion imaging by dynamic light scattering.* Biomedical Engineering, IEEE Transactions on, 1993. **40**(4): p. 309-316.
83. Nilsson, G.E., Tenland, T., and Öberg, P.A., *Evaluation of a laser Doppler flowmeter for measurement of tissue blood flow.* IEEE Trans Biomed Eng, 1980. **27**(10): p. 597-604.
84. Fullerton, A., Stucker, M., and Wihelm, K., *Guidelines for visualization of cutaneous blood flow by laser Doppler perfusion imaging.* Contact Dermatitis, 2002. **46**(3): p. 129.
85. Ahn, H., Ekroth, R., Nilsson, G., and Svedjeholm, R., *Assessment of myocardial perfusion with laser Doppler flowmetry. An experimental study on porcine heart.* Scand J Thorac Cardiovasc Surg, 1988. **22**(2): p. 145-8.
86. Haberl, R.L., Heizer, M.L., Marmarou, A., and Ellis, E.F., *Laser-Doppler assessment of brain microcirculation: effect of systemic alterations.* American Journal of Physiology, 1989. **256**(4 Pt 2): p. H1247-54.
87. Nilsson G., S.G., Strömberg T., Wårdell K., *Laser Doppler perfusion monitoring and imaging*. Biomedical photonics handbook, ed. Vo-Dinh, T. 2003: CRC press LLC.

88. Karlsson, M., Casimir-Ahn, H., Lönn, U., and Wårdell, K., *Analysis and processing of laser Doppler perfusion monitoring signals recorded from the beating heart.* Medical and Biological Engineering and Computing, 2003. **41**(3): p. 255-262.
89. Schmidt, F.E.W., *Development of a time-resolved optical tomography system for neonatal brain imaging*, in *Department of Medical Physics and Bioengineering*. 1999, University College London: London.
90. Edward, A., *The pigments and color of living human skin.* American Journal of Anatomy, 1939. **65**(1): p. 1-33.
91. Eggert, H.R. and Blazek, V., *Optical properties of human brain tissue, meninges, and brain tumors in the spectral range of 200 to 900 nm.* Neurosurgery, 1987. **21**(4): p. 459-64.
92. Lin, W.C., Toms, S.A., Motamedi, M., Jansen, E.D., and Mahadevan-Jansen, A., *Brain tumor demarcation using optical spectroscopy; an in vitro study.* J Biomed Opt, 2000. **5**(2): p. 214-20.
93. Eriksson, O. and Wårdell, K., *Optical changes as a marker for lesion size estimation during radio frequency ablation: a model study.* Proceedings of SPIE, 2003. **4254**: p. 164.
94. Villringer, A. and Chance, B., *Non-invasive optical spectroscopy and imaging of human brain function.* Trends Neurosci, 1997. **20**(10): p. 435–442.
95. Eriksson, O., Backlund, E.-O., Lundberg, P., Lindstam, H., Lindström, S., and Wårdell, K., *Experimental radiofrequency brain lesions: a volumetric study.* Neurosurgery, 2002. **51**(3): p. 781-788.
96. Eriksson, O., Wårdell, K., Bylund, N.E., Kullberg, G., and Rehncrona, S., *In vitro evaluation of brain lesioning electrodes (Leksell®) using a computer-assisted video system.* Neurol Res, 1999. **21**(1): p. 89-95.
97. Wren, J., Loyd, D., Andersson, U., and Karlsson, R., *Thermally induced convective movements in a standard experimental model for characterization of lesions prior to radiofrequency functional neurosurgery.* In press, 2007.
98. Wårdell, K., Blomstedt, P., Richter, J., Antonsson, J., Eriksson, O., Zsigmond, P., Bergenheim, A.T., and Hariz, M.I., *Intracerebral microvascular measurements during DBS-implantation using laser Doppler perfusion monitoring.* Submitted, 2007.
99. Felix, B., Leger, M.E., Albe-Fessard, D., Marcilloux, J.C., Rampin, O., and Laplace, J.P., *Stereotaxic atlas of the pig brain.* Brain Res Bull, 1999. **49**(1-2): p. 1-137.
100. Dam, J., Dalgaard, T., Fabricius, P., and Andersson-Engels, S., *Multiple polynomial regression method for determination of biomedical optical properties from integrating sphere measurements.* Appl. Opt, 2000. **39**(7): p. 1202-1209.
101. Dam, J.S., Yavari, N., Sorensen, S., and Andersson-Engels, S., *Real-time absorption and scattering characterization of slab-shaped turbid samples obtained by a combination of angular and spatially resolved measurements.* Appl Opt, 2005. **44**(20): p. 4281-90.
102. Larsson, M., Steenbergen, W., and Stromberg, T., *Influence of optical properties and fiber separation on laser doppler flowmetry.* J Biomed Opt, 2002. **7**(2): p. 236-43.
103. Qian, Z., Sunder, S.V., Yeqing, G., Giller, C.A., and Liu, H.L., *"Look-ahead distance" of a fiber probe used to assist neurosurgery: Phanton and Monte Carlo study.* Optics express, 2003. **11**(16): p. 1844-1855.
104. De Vita, E., Bainbridge, A., Cheong, J.L., Hagmann, C., Lombard, R., Chong, W.K., Wyatt, J.S., Cady, E.B., Ordidge, R.J., and Robertson, N.J., *Magnetic resonance imaging of neonatal encephalopathy at 4.7 tesla: initial experiences.* Pediatrics, 2006. **118**(6): p. 1812-21.

105. Choi, J.H., Wolf, M., Toronov, V., Wolf, U., Polzonetti, C., Hueber, D., Safonova, L., Gupta, R., Michalos, R., Mantulin, W., and Gratton, E., *Noninvasive determination of the optical properties of adult brain: near-infrared spectroscopy approach.* Journal of Biomedical Optics, 2004. **9**(1): p. 221-229.